



HAL
open science

Earth's volatile accretion as told by Cd, Bi, Sb and Tl core-mantle distribution

E. Kubik, J. Siebert, I. Blanchard, A. Agranier, B. Mahan, F. Moynier

► **To cite this version:**

E. Kubik, J. Siebert, I. Blanchard, A. Agranier, B. Mahan, et al.. Earth's volatile accretion as told by Cd, Bi, Sb and Tl core-mantle distribution. *Geochimica et Cosmochimica Acta*, 2021, 306, pp.263-280. 10.1016/j.gca.2021.02.017 . insu-03590028

HAL Id: insu-03590028

<https://insu.hal.science/insu-03590028>

Submitted on 2 Aug 2023

HAL is a multi-disciplinary open access archive for the deposit and dissemination of scientific research documents, whether they are published or not. The documents may come from teaching and research institutions in France or abroad, or from public or private research centers.

L'archive ouverte pluridisciplinaire **HAL**, est destinée au dépôt et à la diffusion de documents scientifiques de niveau recherche, publiés ou non, émanant des établissements d'enseignement et de recherche français ou étrangers, des laboratoires publics ou privés.



Distributed under a Creative Commons Attribution - NonCommercial 4.0 International License

1 **Earth's volatile accretion as told by Cd, Bi, Sb and Tl**
2 **core–mantle distribution**

3 E. Kubik^{1,*}, J. Siebert^{1,2}, I. Blanchard³, A. Agranier⁴, B. Mahan⁵, F. Moynier¹.

4

5 ¹Institut de Physique du Globe de Paris, Université de Paris, CNRS, 1 Rue Jussieu, 75005 Paris,
6 France

7 ²Institut Universitaire de France, Paris, France

8 ³Bayerisches Geoinstitut, University of Bayreuth

9 ⁴Institut Universitaire Européen de la Mer, Université de Brest

10 ⁵James Cook University, Queensland, Australia

11 *kubik@ipgp.fr

12 **Abstract**

13 The timing and origin of volatile elements accretion on Earth has been and continues to be key
14 questions, despite intense research scrutiny. Two end-member scenarios are usually proposed in which
15 (1) volatile elements were delivered during the main phase of Earth's accretion and underwent
16 subsequent core–mantle differentiation, or (2) Earth accreted from largely dry and volatile-depleted
17 material, with late addition of volatile-rich material after differentiation. Studying the behavior of
18 elements that are both volatile and siderophile in a metal–silicate equilibrium can help discriminate
19 between those two scenarios by deconvolving the effect of siderophile processes such as the Earth's
20 differentiation from the effect of volatile processes. We report high-pressure and high-temperature
21 metal–silicate equilibrium experiments that are used to trace the behavior of four moderately volatile
22 and siderophile elements: Cd, Bi, Sb and Tl. Experiments were performed in piston cylinder and
23 multianvil presses between 2 and 20 GPa, from 1700 to 2600 K, in order to study the partitioning
24 behavior of these elements, including the relative influence of pressure, temperature, oxygen fugacity
25 (fO_2), and composition. Our results indicate that Cd, Bi, Sb and Tl partitioning coefficients are largely
26 controlled by changes in temperature, pressure, fO_2 and the S content of the metal phase. The pressure
27 effect on Tl and Bi partitioning is measured for the first time and improves significantly the
28 knowledge of Bi and Tl behaviour during core formation. Core formation modelling was used to
29 reconcile the experimental data with observed abundances for different accretion scenarios.
30 Homogeneous accretion with full core–mantle equilibration induces a massive segregation of Bi, Sb
31 and Tl in the core, preventing reproduction of observed present-day mantle abundances. We find that a
32 scenario in which the volatile elements are accreted in the last 10–20% of the Earth's accretion is the
33 most suitable accretion process that is able to explain the abundances of Cd, Bi, Sb and Tl in Earth's
34 mantle. Partial core–mantle equilibration is necessary to reproduce Bi and Tl abundances. Our
35 partitioning data also suggests that a 0.5% chondritic late veneer may account for the Bi abundance
36 measured in the bulk silicate Earth. These observations corroborate a growing wealth of evidence in
37 support of this schematic heterogeneous accretion pathway.

38 1. Introduction

39 The presence of active plate tectonics, liquid ocean and life, make the Earth unique compared to any
40 other terrestrial planets of the solar system. The origin of volatile elements—which are crucial to the
41 development of life on Earth—is a hotly debated topic. The depletion in volatile elements of the
42 Earth’s mantle could be due to (1) volatile loss by syn- and post-accretional volatilisation, and/or to
43 (2) incomplete condensation of the solar nebula (Albarède, 2009).

44 Volatile loss on Earth has been largely argued against by studies reporting a lack of heavy isotope
45 enrichment in the Earth’s mantle compared to primitive meteorites (Humayun and Clayton 1995; Luck
46 et al., 2005; Pringle et al., 2017; Pringle and Moynier, 2017; Sossi et al., 2017; Tuller-Ross et al.,
47 2019; Varas-Reus et al., 2019; Wang and Jacobsen, 2016), although small isotopic fractionations
48 reported for Mg (Hin et al., 2017) and Si (e.g. Pringle et al., 2014; Young et al., 2019) suggest
49 volatilisation may have happened. The Mn/Na ratio, which is sensitive to post-nebular volatilisation
50 and is chondritic in the bulk Earth, provides an additional argument for limited volatile loss during or
51 after Earth’s accretion (O’Neill and Palme, 2008; Siebert et al., 2018), favoring incomplete
52 condensation of the solar nebula as the main process explaining the volatile depletion on Earth. This
53 study aims at discriminating between several plausible accretion scenarios that could produce the
54 observed volatile elements pattern of the Earth’s mantle:

55 (1) “Dry accretion”, where the Earth largely accreted from dry material, devoid of volatile elements.
56 The solar system temperature during that period may have been too high to allow the condensation of
57 volatile elements (Albarède, 2009), supporting this scenario. The volatiles are brought after core
58 formation ceased, as a late veneer of chondritic composition (Albarède et al., 2013; Budde et al., 2019;
59 Dauphas et al., 2017; O’Neill, 1991).

60 (2) “Wet accretion”, on the other hand, is accretion from building blocks that are partially volatile
61 depleted, such as chondritic material(s). The elements are segregated between core and mantle
62 according to their siderophility during differentiation, which explains the abundances of elements in
63 the Earth’s mantle (Righter et al., 2017b; Wood and Halliday, 2010), potentially associated with
64 volatile loss (Hin et al., 2017; Norris and Wood, 2017; Pringle et al., 2014).

65 (3) In an intermediate scenario, Earth is accreted from compositionally heterogeneous material, and
66 the bulk of its volatile element inventory is brought in the last stages of accretion and differentiation.
67 As proposed by [Braukmüller et al \(2019\)](#), the volatile elements on Earth could originate from 10 to 15
68 wt.% of CI-like material brought towards the end of the main phases of Earth's accretion. This stage
69 could have been associated with the formation of a volatile-rich liquid sulfide matte that subsequently
70 mixed into the core ([O'Neill, 1991](#); [Savage et al., 2015](#); [Schonbachler et al., 2010](#)).

71 By studying the metal–silicate partitioning behavior of elements that are both volatile and siderophile,
72 the effect of the Earth's differentiation can be isolated from the effect of volatile processes, helping to
73 discriminate between the three main volatile accretion scenarios.

74 This study focuses on four moderately volatile and siderophile elements (MSVEs), which are depleted
75 in the Earth's mantle compared to lithophile volatile elements as a consequence of their segregation
76 into the core during differentiation ([Lodders, 2003](#); [Wasson et al., 1988](#); [Wood et al., 2019](#)).

77 Experimental studies of MSVE behaviour at metal–silicate equilibrium at high pressure and high
78 temperature can be used to characterise the siderophilicity of such elements and infer the effect of
79 differentiation on their observed abundances in the Earth's mantle (e.g. [Ballhaus et al., 2017](#);
80 [Blanchard et al., 2015](#); [Corgne et al., 2008](#); [Mahan et al., 2017](#); [Righter et al., 2017a](#); [Siebert et al.,](#)
81 [2011](#); [Steenstra et al., 2019](#); [Suer et al., 2017](#)). Comprehensive parameterisation of metal–silicate
82 partitioning includes the effect of pressure, temperature, fO_2 , metal and silicate composition. Such
83 parameterisation can be used as input in core formation models, where the partitioning is reconstructed
84 at each step of the Earth's accretion at the predicted pressure and temperature conditions of the Earth's
85 differentiation. These models are used to test various accretion scenarios in an attempt to reconcile
86 experimentally determined partitioning behaviors of elements with their observed abundances in the
87 Earth's mantle (e.g. [Blanchard et al., 2015](#); [Rubie et al., 2011](#); [Wade and Wood, 2005](#)). The results of
88 those models can then be compared to natural observation and used to isolate the most likely accretion
89 scenarios.

90 This study is focused on experimental characterisation of the partitioning behavior of Cd, Bi, Sb, and
91 Tl in a metal–silicate equilibrium. These elements are MSVEs with condensation temperatures of 652,
92 746, 979 and 532 K respectively ([Lodders, 2003](#)), recently reappraised to 502, 480, 890 and 365 K

93 (Wood et al., 2019) in particular by including recent halogen abundances adjustment (Clay et al.,
94 2017). The fact that they are affected by core–mantle differentiation as well as volatile processes
95 makes them good tracers of volatile accretion. Cadmium metal–silicate partitioning data has been
96 reported in several studies (e.g. Wang et al., 2016; Wood et al., 2014) with very different conclusions,
97 ranging from Cd mantle abundance being fully explained by core formation (Richter et al., 2017a,
98 2019), to not at all (Ballhaus et al., 2013). This could be the consequence of the scarcity of high-
99 pressure experiments permitting to observe and quantify other operative effects such as pressure.
100 Bismuth and thallium metal–silicate partitioning have never been measured above 3 GPa, meaning
101 that the pressure effect on their partitioning has never been constrained. Bismuth abundance in the
102 bulk silicate Earth (BSE) has been explained based on low-pressure data, to be controlled by core
103 formation (Richter et al., 2017a) possibly associated with segregation in a sulfide matte (Richter et al.,
104 2019,2020), but models including the pressure effect on the Bi partitioning could lead to significantly
105 different conclusions. Also based on low-pressure experiments, Tl abundances in the BSE have been
106 explained by late accretion (Ballhaus et al., 2013) or sulfide segregation (Wood et al., 2008, 2014).
107 However, novel insights on the pressure effect on the Tl partitioning could help refine the associated
108 core formation models. Existing data of Sb partitioning include a majority of experiments below 4
109 GPa (Steenstra et al., 2017; Steenstra et al., 2020a,b), though some higher-pressure experiments are
110 reported (Vogel et al., 2018), and lead to a variety of proposed scenarios that may explain the Sb
111 abundance in the BSE: core formation alone (Richter et al., 2009, 2017a,b), possibly including
112 equilibration with a sulfide liquid (Wood et al., 2014). Further parameterisation of the Sb partitioning
113 between metal and silicate may help to better understand the processes that produced the observed Sb
114 abundance in the Earth’s mantle.

115 We report novel partitioning data for 17 experiments performed at high pressure and high temperature.
116 Combined with literature data, they enhance our collective comprehension of the behavior of these
117 elements, in particular by widening the range of pressure investigated in this type of experiments.
118 Subsequent parameterisation was used for extrapolation to conditions relevant to Earth’s
119 differentiation, and has been input into core formation models to explore the partitioning behaviour of

120 Cd, Bi, Sb and Tl along a range of plausible volatile accretion trajectories and propose coherent story
121 for the distribution of these MVSEs during Earth's accretion.

122 **2. Experimental and analytical methods**

123 **2.1. Starting materials**

124 Experiments were prepared with two different starting materials made of 30:70 metal and silicate
125 powder mixtures (Table 1). A natural MORB was used as the silicate fraction. The metal fraction was
126 added to the silicate as pure powders of Fe and FeS. Tin was also added to the starting mixtures, and
127 will not be further discussed here as it will be the focus of a distinct publication. The mixture was then
128 doped at a 1 *wt.%* level with elements of interest and all components were combined in an agate
129 mortar after weighing, and the bulk subsequently mixed and crushed together until obtaining a
130 homogeneous mixture.

131 **2.2. Piston cylinder experimentation**

132 Five experiments were performed with a 150-tons end-loaded piston cylinder press at the Institut
133 Physique du Globe de Paris (IPGP). They were all performed in ½" cell assemblies at 2 GPa and from
134 1773 to 2273 K. The duration of each run was chosen carefully with respect to the temperature in
135 order to reach elemental equilibrium between molten metal and silicate melt while minimising the
136 chemical reactions with the capsule (Corgne et al., 2008; Siebert et al., 2011). Prior to the run, a MgO
137 capsule was filled with starting material and packed, and the capsule was placed inside a talc–pyrex
138 assembly (Siebert et al., 2011). The temperature of the sample was measured during the experiment
139 using a type D thermocouple (W₉₇Re₃/W₇₅Re₂₅) previously placed in contact with the lid of the
140 capsule. Samples were quenched by terminating heating. Representative pieces of metal and silicate
141 were mechanically selected under magnifying glass, mounted in resin and carefully polished for
142 scanning electron microscopy (SEM) observation, and electron microprobe (EPMA) and laser ablation
143 (LA-ICPMS) measurements.

144

2.3. Multianvil experimentation

145 Twelve multianvil experiments were performed at Bayerisches Geoinstitut using a 5000-ton Zwick
146 and a 1000-ton Hymag multianvil apparatus from 7 to 20 GPa. Pressure media consisted of MgO
147 octahedra with 18 and 25 mm edges (Rubie, 1999; Frost et al., 2004). Cubic tungsten carbide anvils
148 with 15, 11 and 8 mm truncations (25/15, 18/11 and 18/8 configurations) were used to apply pressure
149 to the sample along three primary axes. The starting material was contained in MgO single-crystal
150 capsule and lid. In order to minimise temperature gradients, a stepped LaCrO₃ heater was used. During
151 the experiment, the sample temperature was monitored using a type D W₉₇Re₃/W₇₅Re₂₅ thermocouple.
152 The experimental conditions are summarised in Table 4. The whole samples were mounted in resin
153 and polished until exposure of a significant surface of metal and silicate material for SEM (see
154 Supplementary information), EPMA and LA-ICPMS analysis. Further details about the experimental
155 procedures and pressure calibration of piston cylinder and multianvil presses used in this study can be
156 found in the Supplementary information.

157

2.4. Electron microprobe measurements

158 EPMA measurements were performed using a CAMECA SX Five electron microprobe (CAMPARIS,
159 Université Pierre et Marie Curie). Polished and mounted samples were evenly carbon coated prior to
160 analysis. A selection of major and trace elements was resolved in both metal and silicate phases (Table
161 2) using an accelerating voltage of 15 keV and a beam current of 300 nA. Counting times were chosen
162 as follows: 10-20 s for major and 20-90 s for trace elements. To prevent heterogeneities induced by
163 quench textures from affecting the measurements, 30 µm rasters were used instead of points to
164 improve the analytical statistics (see Supplementary information). No compositional zonation was
165 found across the samples presented in this study, advocating for equilibrium achievement.

166

2.5. Laser ablation ICP-MS measurements

167 LA-ICPMS measurements were performed on the silicate phases of the experiments of this study in
168 order to constrain the concentration of elements of interest in lower concentration than EPMA
169 detection limits (Table 2). Laser ablation analyses were performed using an Element XR high-
170 resolution mass spectrometer (Université de Brest) coupled to a 193 nm Compex Pro 102 Coherent

171 Laser system. The laser was set to a 15J/cm² output and a 10 Hz frequency. A 90- μ m beam was used
172 to vaporise a significant amount of sample, and 3 to 8 measurements were performed and averaged on
173 each sample (Table 4). A helium flux was used to carry the ablated particles that were mixed with
174 argon before entering the plasma. Data calibration was computed using both Mg concentrations
175 previously measured by EPMA as internal standardisation and standard interpolations by measurement
176 of silicate standards NIST610, NIST612 and NIST614. Data corrections were carried out using
177 GLITTER software to correct for deadtime ([Van Achterbergh et al., 1999](#)) and subsequent manual
178 data reduction was done to subtract the background and normalise to Mg for the last cycles.

179 **3. Results**

180 **3.1. Petrography**

181 Petrological observation of silicate phases shows homogeneous melt presenting dendritic quenched
182 olivine and pyroxene crystals due to reaction with the MgO capsule. Metal phases consist of a single
183 metal sphere with a diameter of roughly 1 mm in piston cylinder runs and 500 μ m in multianvil runs.
184 Quench textures can be observed on the sections of these spheres. These petrological observations (see
185 Supplementary information) indicate that the starting material was fully melted at superliquidus
186 temperatures allowing coalescence of the liquid metal and equilibrium achievement.

187 **3.2. Elemental compositions**

188 All elemental concentrations from EPMA and LA-ICPMS are presented in Table 2. In the silicate
189 phase of the experiments, the MgO content ranges from 15.4 to 37 *wt.%* and SiO₂ from 30.2 to 48.5
190 *wt.%*. The combination of EPMA and LA-ICPMS allowed to measure the wide range of
191 concentrations of the studied elements: 900 to 4000 ppm for Cd, 4 to 200 ppm for Bi, 1 to 1400 ppm
192 for Sb and 600 to 6000 ppm for Tl. We note that although E345 yields a low total by EPMA analysis,
193 which may indicate contamination from the outer assembly, the partitioning data of this single
194 experiment was found very consistent with the rest of our dataset as well as literature data ([Richter et](#)
195 [al., 2017b](#)), especially for Sb and Bi, and was therefore included in the dataset presented here.

196 Iron is the main component of the metallic phase with 60 to 90 wt.%. The S content ranges from 0.1 to
 197 20 wt.%. Concentrations of the elements of interest in Fe-rich phase range well above EPMA detection
 198 limits, as follows: 0.03 to 2 wt.% for Cd, 0.04 to 3.5 wt.% for Bi, 1.8 to 3.5 wt.% for Sb and 0.01 to 2.3
 199 wt.% for Tl. Experiments presenting Tl concentrations close to EPMA detection limit (e.g. Z1825)
 200 were discarded for further calculations.

201 Silicate and metallic phases were found compositionally homogeneous after thorough SEM
 202 observation and EPMA analyses. Oxygen fugacity, calculated with respect to the iron-wüstite (IW)
 203 buffer (Equation 1), varies from -2.8 to -1.7 in the experiments. In this equation, the activities are
 204 taken equal to the molar fractions based on a negligible predicted effect of the variations of
 205 composition amongst the experiments (i.e. calculated fO_2 would lead to a change of ~0.2 log units
 206 when considering activity model of iron in metal for a putative composition of 30 wt.% S in the
 207 metal).

$$\Delta IW = 2 \cdot \log \frac{X_{FeO}^{silicate}}{X_{Fe}^{metal}}$$

Equation 1

3.3. Metal–silicate partitioning

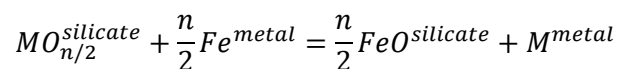
211 The distribution of an element M of valence state n between metal and silicate at equilibrium
 212 conditions can be expressed with the partition coefficient:

$$D_M = \frac{X_M^{metal}}{X_{MO_{n/2}}^{silicate}}$$

Equation 2

215 where X_i are the mole fractions of element M or its oxide in the metal and silicate phases.

216 The equilibrium of M between metal and silicate can also be represented as a chemical exchange redox
 217 reaction:



Equation 3

220 The exchange coefficient K of this reaction will allow to quantify the partitioning of element M
 221 independently of fO_2 , simplifying the study of the effect of other parameters such as pressure,
 222 temperature and composition:

$$223 \quad K = \frac{(a_{FeO}^{silicate})^{n/2} \cdot (a_M^{metal})}{(a_{MO_{n/2}}^{silicate}) \cdot (a_{Fe}^{metal})^{n/2}}$$

224 Equation 4

225 where a_i are the activities of the different components, such as $a_i = \gamma_i X_i$, where γ_i is the activity
 226 coefficient and X_i is the mole fraction:

$$227 \quad \log K = \log \frac{(X_{FeO}^{silicate})^{n/2} \cdot (X_M^{metal})}{(X_{MO_{n/2}}^{silicate}) \cdot (X_{Fe}^{metal})^{n/2}} + \log \frac{\gamma_M^{metal}}{(\gamma_{Fe}^{metal})^{n/2}} + \log \frac{(\gamma_{FeO}^{silicate})^{n/2}}{\gamma_{MO_{n/2}}^{silicate}}$$

228 Equation 5

$$229 \quad \log K = \log \frac{D_M}{(D_{Fe})^{n/2}} + \log \frac{\gamma_M^{metal}}{(\gamma_{Fe}^{metal})^{n/2}} + \log \frac{(\gamma_{FeO}^{silicate})^{n/2}}{\gamma_{MO_{n/2}}^{silicate}}$$

230 Equation 6

$$231 \quad \log K = \log K_d^M + \log \frac{\gamma_M^{metal}}{(\gamma_{Fe}^{metal})^{n/2}} + \log \frac{(\gamma_{FeO}^{silicate})^{n/2}}{\gamma_{MO_{n/2}}^{silicate}}$$

232 Equation 7

233 The term K_d^M can be calculated for each experiment as it depends on molar concentrations of M and Fe
 234 in the metal and silicate phases. The determination of the valence state of M is essential for the
 235 calculation of the equilibrium constant and further parameterisation of the partitioning. The preferred
 236 valence state for Cd is 2+ in numerous previous studies (Richter et al., 2017a, 2019; Wood et al.,
 237 2014). It can be demonstrated that $\log D_M$ is a function of $\frac{n}{4} \log fO_2$, allowing to calculate the valence
 238 state from a selection of experiments that are similar in pressure, temperature and composition over a
 239 sufficient range of fO_2 (Siebert et al., 2011). Our data combined with literature data allows to provide
 240 such an estimation of the valence state of Cd over more than two log units of fO_2 (Figure 1). The slope
 241 of the regression line is equal to 0.5, which corresponds to a 2+ valence state. The scarcity of the data
 242 and insufficient oxygen fugacity range prevents from demonstrating the valence state of Bi, Sb and Tl
 243 by the same method as that of Cd on Figure 1. However, Sb has been studied assuming largely a 3+

244 valence state (Richter et al., 2009, 2017a,b; Steenstra et al., 2017; Vogel et al. 2018; Wood et al.,
245 2014) and 3+ was also favored in this study. Bismuth partitioning was also parameterised as a trivalent
246 cation in agreement with previous studies (Richter et al., 2017a, 2019), and Tl as a monovalent cation
247 (Wood et al., 2008, 2014). XANES studies are needed in order to quantitatively determine the valence
248 state of these elements in silicate melts.

249 The partitioning of Cd, Bi, Sb and Tl represented by the exchange coefficient $\log K_d$ defined in
250 Equation 7 is presented on Figure 2 as a function of reciprocal temperature. According to our dataset,
251 Cd partitioning (Figure 2a) presents no resolvable effect of temperature or pressure. Although it has
252 been suggested that there could be a positive (Ballhaus et al., 2013; Steenstra et al., 2020b) or negative
253 (Richter et al., 2017a) effect of temperature on Cd partitioning, the wide range of temperatures
254 presented in Figure 2a combined with the $\log K_d$ formalism used in this study do not show this effect.
255 Experiments performed below 19 GPa and containing significant amounts of S in their metal present
256 enhanced $\log K_d$, suggesting a positive effect of S at those conditions. On Figure 2b which displays
257 $\log K_{dBi}$, temperature notably decreases the partitioning and pressure has a strong positive effect on
258 $\log K_d$, as recently observed in Richter et al. (2020). A similar pattern is observed from $\log K_{dSb}$
259 (Figure 2c). Sulfur has a positive effect on Bi partitioning of experiments at 2 GPa whereas S-bearing
260 experiments at higher pressures present similar $\log K_d$ as S-free experiments of similar conditions. For
261 Sb, all S-bearing experiment present lower partitioning than their S-free analogs, suggesting a negative
262 effect of S, in accordance with previous studies (e.g. Wood et al., 2014). Pressure and temperature
263 both have a strong and positive effect on $\log K_{dTl}$ (Figure 2d). A discrepancy on the S effect can be
264 observed on Figure 2d where S-bearing low-pressure experiments present higher partitioning than S-
265 free ones whereas above 10 GPa S-bearing experiments present lower partitioning than their S-free
266 analogues.

267 **4. Discussion**

268 **4.1. Equilibrium achievement**

269 Achievement of equilibrium between metal and silicate is critical for accurate characterisation and
270 parameterisation of the studied elements at such conditions. Steenstra et al. (2017) report time series

271 experiments at 1783 K for Cd and Sb, showing complete equilibration of the experiments after 15
 272 minutes at such temperature. We therefore applied similar—and sufficient—time durations allowing
 273 complete fusion of the sample (Thibault and Walter, 1995), as well as thorough petrographic
 274 characterisation showing homogeneous phases, were achieved in this study. Our data presents
 275 overarching trends that can be described thermodynamically, thus providing further evidence of
 276 equilibrium.

277 4.2. Metal–silicate partitioning of MSVEs and Earth accretion

278 4.2.1. Thermodynamic parameterisation

279 Parameter $\log K_d$ defined in Equation 7 was calculated for Cd, Bi, Sb and Tl in each experiment and
 280 reported in Table 2 and presented in Figure 2. The ratio of oxide activity coefficients was neglected as
 281 it is predicted to have little effect on the equilibrium constant, especially for low—below 4+—valence
 282 state elements (Wade and Wood, 2005). $\log K_d$ can be expressed as follows:

$$283 \log K_d = a + b \cdot \frac{1}{T} + c \cdot \frac{P}{T} - \log \frac{\gamma_M^{metal}}{(\gamma_{Fe}^{metal})^{n/2}}$$

284 Equation 8

285 The constants a , b and c reported in Table 3 were computed using the least-squares multivariate linear
 286 regression method from measurements on experiments of this study and associated literature with a
 287 metal devoid of S, Si and C. These parameters were used to calculate the regression lines displayed in
 288 Figure 2 and 3.

289 The activity coefficients representing the effect of the metal composition on the partitioning were
 290 calculated by using the partitioning of S-bearing experiments:

$$291 \log K - \log K_D = \log \left(\frac{\gamma_M^{metal}}{(\gamma_{Fe}^{metal})^{n/2}} \right)$$

292 Equation 9

293 The activity coefficients γ_M^{metal} and γ_{Fe}^{metal} were deduced using the interaction parameter approach
 294 developed by Ma (2001):

$$295 \log K_D = \log \frac{D_M}{(D_{Fe})^{n/2}} = a + b \cdot \frac{1}{T} + c \cdot \frac{P}{T} - \log \gamma_M^0 + \varepsilon_M^M \cdot \log(1 - x_M) + \varepsilon_M^S \cdot \log(1 - x_S) + \left(\frac{n}{2} - 1\right) \cdot \varepsilon_S^S \cdot (x_S + \log(1 - x_S))$$

296 Equation 10

297 where ε_j^i represents interaction parameter of i on j , and γ_M^0 the activity coefficient of M . ε_M^S is the
 298 interaction parameter representing the effect of the presence of S on the activity of M . ε_M^S was fitted to
 299 the experimental dataset for all four elements using Equation 10 and reported in Table 3. It should be
 300 noted that the ε_M^S computed from our dataset are consistent with other estimates for Cd and Tl (Wood
 301 et al., 2014), although we find a larger effect of S on Sb partitioning than previously estimated. Our
 302 results indicate that ε_M^S is pressure-dependent for Cd, Bi and Tl. This is in good agreement with other
 303 studies detecting an effect of pressure on interaction coefficients ε_M^S (Wang et al., 2016) and ε_M^{Si}
 304 (Steenstra et al., 2020a) for several siderophile elements. Such pressure effect could be explained by
 305 structural transitions of liquid metal at pressures above 5 GPa (e.g. Morard et al., 2007; Siebert et al.,
 306 2004; Sanloup et al., 2011) or in the silicate (e.g. Lee et al., 2003). Values of $\log K$, calculated for all
 307 experiments of the dataset, are shown in Figure 3. This expression of M metal–silicate partitioning
 308 only displays the effect of pressure and temperature. S-bearing experiments are corrected for their S
 309 effect and show similar partitioning to experiments of same PT conditions that are devoid of S.

310 4.2.2. Core formation models

311 Core formation modeling is used to assess the partition coefficient of an element at each incremental
 312 step of a differentiated planetary body’s accretion (Rubie et al., 2015). The intended purpose is to
 313 compare the final partition coefficient obtained to the observed partitioning of an element in a
 314 planetary body of interest. By testing multiple accretion scenarios and their effects on the distribution
 315 of the element of interest, it is possible to propose one or a variety of scenarios that can account for the
 316 observed abundance of an element in the mantle of a differentiated planet.

317 The experimentally computed regression parameters that describe the behavior of Cd, Bi, Sb and Tl in
 318 a metal–silicate equilibrium (Table 3) were used to recalculate the partitioning over the course of
 319 Earth’s accretion, simulating several different plausible scenarios, using the following equation:

$$320 \quad \log D_M = \log K_d^M - \frac{n}{2} \cdot \log \left(\frac{x_{FeO}}{x_{Fe}} \right)$$

321 Equation 11

322 We used continuous core formation models (Wade and Wood, 2005) in which the evolution of
 323 pressure and temperature conditions at the base of a deep magma ocean was reconstructed over the

324 course of the accretion, as a function of the accreted fraction. Planetesimals and differentiated
325 planetary embryos of increasing sizes are brought one by one to form the planet. The fO_2 of present-
326 day core–mantle equilibrium was used (IW-2.3) during the accretion for all models. All presented
327 models were computed with 1.9 wt.% of S in the core of the Earth and differentiated embryos, in
328 agreement with multiple estimates (e.g. [McDonough et al., 2003](#); [Suer et al., 2017](#)). Other light
329 elements likely contribute to the composition of the Earth’s core (e.g. [Badro et al., 2015](#)), up to 10% of
330 its mass, and could have an effect on the partitioning of the four elements studied. However, the
331 determination of such effects falls beyond the scope of this publication, as they need to be
332 systematically investigated in future work. Parameter k , defined as the fraction of the core of the
333 accreted embryo that equilibrates with the mantle of the proto-Earth, is used to simulate several
334 degrees of equilibration efficiency. Fluid dynamics analog experiments showed that full equilibration
335 of an impactor’s core with the proto-planet’s core necessitates the metal of the impactor’s core to
336 break down to small size droplets and to segregate into the core of the planet, which is less efficient
337 with increasing impactor size. This effect can be modeled using parameter ε ([Deguen et al., 2014](#))
338 which includes the effect of the mass of silicate that is dragged towards the core along with the metal
339 when metal segregation occurs, preventing full equilibration. The formalism established by [Deguen et](#)
340 [al. \(2014\)](#) was used to model the efficiency of the equilibrium with more accuracy.

341 Homogeneous models, where the elements involved—Cd, Bi, Sb, Tl and S—are present in the same
342 concentrations in the accreted material over the course of the accretion, were computed for each of the
343 four elements of interest. A heterogeneous accretion scenario was also modeled, in which the delivery
344 of the volatile elements is concentrated in the later part of the main phases of Earth’s accretion, before
345 core segregation ceased, as proposed in recent studies ([Braukmüller et al., 2019](#); [Suer et al., 2017](#)). We
346 also tested the possibility of a late veneer, consisting of the late accretion of a limited amount of
347 chondritic material which may have been brought after core formation ended, and would therefore be
348 mixed in the mantle with no equilibration with the core. The late veneer is a process best known for
349 explaining the platinum group elements abundances in the Earth’s mantle, which are orders of
350 magnitude higher than their predicted abundances by core segregation, given their highly siderophile
351 behavior (e.g. [Holzheid et al., 2000](#); [Day et al., 2016](#)).

352 Results from the core formation models computed in this study (Figure 4) were compared to
353 estimations of the core–mantle partition coefficient of Cd, Bi, Sb and Tl, which are based on natural
354 samples measurements. For each element, this estimation is calculated by assuming that the MSVE
355 accreted in similar relative abundance to a lithophile element of similar volatility. In this framework,
356 the additional depletion of the MSVE relative to the canonical volatile lithophile trend is attributed to
357 its segregation into the core. As this is a quantitative approach, each element’s depletion can be
358 calculated and used as to estimate the abundance of a given MSVE in the Earth’s core. Combined with
359 the BSE abundance estimates, an apparent core–mantle partition coefficient can be constituted (see
360 Supplementary information). Each of Cd, Bi, Sb and Tl was paired with the lithophile element of
361 closest condensation temperature (Table 4). We provide two estimates, one using condensation
362 temperatures T_{50} from [Lodders \(2003\)](#) and a second one using more recent estimates from [Wood et al.](#)
363 [\(2019\)](#), which changes the lithophile reference element for Cd, Bi, Sb, and therefore the core/BSE
364 estimation. We also considered the hockey stick volatile pattern proposed by [Braukmüller et al. \(2019\)](#)
365 which affects Cd, Bi and Tl as their condensation temperatures correspond to the plateau part of the
366 pattern. We used a range including all three of these estimates as the apparent core–mantle value,
367 acting as a “target” for our core formation models.

368 Results from core formation modelling are presented in Figure 4. The effect of S on partitioning
369 determined experimentally is varying with the pressure of equilibrium (Table 3). This was taken into
370 account in the models and the S effect was calculated according to the pressure range when necessary.
371 In calculations considering partial equilibration, D_M is sensitive to the size of the accreted embryos
372 which is why we observe variations on the curves at stages where there is a change of the size of
373 accreted bodies. For Cd, Sb and Tl, a late veneer of 0.5% of the Earth’s mass composed of CI material
374 was found to have negligible effect on the modelled partitioning. Such a process would account for
375 only ~10 wt.% of the abundance of these elements in the Earth’s mantle, and was therefore not
376 included on the corresponding figures. In the case of Bi, for which a 0.5 wt.% late veneer would raise
377 by 16 wt.% its BSE abundance, the effect is larger and was included in the models presented in Figure
378 4b.

379 Experimental Cd partitioning was found to be independent of pressure and temperature conditions,
380 with a positive effect of S on D_{Cd} reported below 18 GPa. This leads to a full match of all the modelled
381 scenarios with the apparent core–mantle value which ranges from 0 to 11.5 (Figure 4a), preventing
382 strong arguments in favour of a scenario compared to another. D_{Cd} evolution for a homogeneous
383 accretion leads to a final partitioning of 3.2 ± 1.4 . However, a heterogeneous scenario with an accretion
384 of the volatiles in the last 10% yields a final D_{Cd} of 5.5 ± 2.3 which is closer to the central estimated
385 value. This is due to the fact that the pressure of equilibration in the last accreted embryo, 10% of
386 Earth’s mass, is inferior to 18 GPa, inducing an effect of S that increases the partitioning. On the
387 contrary, with a scenario of volatile delivery in the last 20%, the final accreted embryo is equilibrated
388 at a pressure above 18 GPa, which means that the effect of S is not considered. The final D_{Cd} is
389 2.7 ± 1.1 and sits further from the central value.

390 The estimated D_{Bi} of the Earth ranges from 1.2 to 28.9 (Table 4). The reconstructed partitioning for a
391 scenario of full equilibration with compositionally homogeneous accretion is more than one order of
392 magnitude higher than the observed value, with a final D_{Bi} of 762 ± 225 (Figure 4b), making this
393 scenario unlikely. A homogeneous scenario with partial equilibration (final $D_{Bi}=129\pm 38$) yields a final
394 partitioning also significantly higher and distinct from the apparent value. It should be noted that a
395 homogeneous accretion with a partial equilibration and a 0.5 wt.% late veneer would not meet the
396 upper limit of the estimated core–mantle value with a final D_{Bi} of 63 ± 19 . When considering an
397 accretion of the volatiles in the last 10 and 20% of the accretion including a 0.5 wt.% late veneer of CI
398 chondrite-like material, the final D_{Bi} is closer to the observed partitioning, with final D_{Bi} of 44 ± 13 and
399 52 ± 15 respectively. When using distinct BSE estimate by [McDonough et al. \(2003\)](#) of 2.5 ± 0.75 ppb,
400 the estimated core–mantle partitioning (31 ± 25) is higher and less consistent with the estimate from
401 [Braukmüller et al. \(2019\)](#) but allows for the modelled accretion of the volatile elements in the last 10%
402 with a 0.5% late veneer to reproduce the estimated partitioning within error, with $D_{Bi}=44\pm 13$. Bismuth
403 abundance in the Earth mantle is not well resolved, but by using multiple existing estimates the only
404 scenario in which this abundance can be accounted for involves a heterogeneous accretion of the

405 volatile elements in the last 10% of Earth's accretion associated to a 0.5 wt.% late veneer of chondritic
406 composition.

407 The core formation models of Sb (Figure 4c) are unique in the sense that for a homogeneous accretion,
408 the scenario with partial equilibration presents a higher final partitioning (80 ± 29) than with a full
409 equilibration (68 ± 25) because of the strong negative effect of S that is undermined by a less efficient
410 equilibration. These two scenarios are higher than the apparent core–mantle D_{Sb} which ranges from 7
411 to 16. Three heterogeneous scenarios are presented here with an accretion of the volatile elements in
412 the last 10, 15 and 20% of the Earth's formation yielding final partition coefficients of respectively
413 4 ± 1 , 12 ± 4 and 20 ± 7 . The 15% late accretion scenario is the best match to the central observed value
414 and the modelled 20% scenario presents a final D_{Sb} that falls within error of estimated core–mantle
415 value.

416 The apparent core–mantle D_{Tl} value ranges from 0.6 to 38. A homogeneous model with full
417 equilibration (Figure 4d) yields a final D_{Tl} of 924 ± 414 , which is significantly higher than the target
418 value, preventing reconciliation of the experimental data with the observed abundances through this
419 scenario. Using a partial equilibration model for the same homogeneous accretion scenario allows to
420 match the observed partitioning with a final D_{Tl} of 8.8 ± 4 . Three heterogeneous accretion models are
421 also presented, with two of them yielding final D_{Tl} within the range of the observed core–mantle
422 value: 3.2 ± 1 for a delivery of volatiles in the last 15% of Earth's accretion and 9.3 ± 4 for a delivery in
423 the last 20%. A scenario of accretion of the volatiles in the last 10% of the Earth's accretion presents a
424 final D_{Tl} lower but within error of the observed value (0.5 ± 0.2).

425 A homogeneous accretion with full equilibration is only compatible with the observed partitioning in
426 the case of Cd, therefore, such a scenario is not well supported by this study. The apparent core–
427 mantle partition coefficients of Cd and Bi are best reproduced in the case of an accretion of the
428 volatiles in the last 10% of the Earth's accretion with a partial equilibrium, although the Cd models do
429 not allow strong conclusions. The abundances of Sb and Tl in the BSE are best modelled in a scenario
430 of accretion of the volatile elements in the last 15–20% of Earth's accretion. The abundances of Cd
431 and Tl could also be explained by a homogeneous accretion with partial equilibration. Although Cd,

432 Sb and Tl apparent partitioning can be explained without including a late veneer, no model would fall
433 in the range of the apparent Bi core–mantle value without a 0.5 wt.% late veneer, in agreement with
434 previous studies based on different geochemical observables (Holzheid et al., 2000; Médard et al.,
435 2015; Suer et al., 2017). Several scenarios could explain the abundances in the Earth’s mantle for most
436 of the elements studied here, however, the most supported scenario includes a partial equilibration and
437 an accretion of the volatile elements in the last 10 to 20% of the Earth’s accretion, before core–mantle
438 equilibration ceased, possibly followed by a 0.5% late veneer composed of CI chondritic material.
439 Such a scenario is also supported by recent studies (Braukmüller et al., 2019; Mahan et al., 2018a,b;
440 Suer et al., 2017). Lastly, our results advocate for partial equilibration over full equilibration
441 (especially for Bi and Tl) which is a result worth mentioning since the efficiency of the core–mantle
442 equilibration is a debated topic (e.g. Deguen et al., 2014; Kendall and Melosh, 2016). It should be
443 noted that several processes that were not included in the models of this study could, when considered
444 and quantified, modify the outcomes of the models. First, the presence of Si in the core could have a
445 strong negative effect on the partitioning of volatile and siderophile elements, as suggested by Righter
446 et al. (2019). In this case, the addition of Si to the core would likely lower the partitioning of the
447 elements, thus influencing the results and conclusions of this study. However, the effect of Si on the
448 partitioning of these elements needs to be carefully addressed, as experiments containing Si-rich metal
449 often lead to the formation of immiscible metallic liquids (e.g. at 1 GPa, Righter et al., 2019) and to
450 the exsolution of nuggets in the silicate melt. Further work dedicated to the study of the effect of Si on
451 the partitioning of these elements are required to confirm the large effects reported in Righter et al.
452 (2019,2020). Furthermore, given their chalcophile behaviour, the Bi and Tl budgets in the Earth’s
453 mantle could be influenced by the formation of a sulphide matte by sulfur saturation towards the end
454 of differentiation (e.g. O’Neill, 1991) which was not considered here but could be modelled in future
455 work with proper characterisation of their sulphide-silicate partitioning.

456

4.3. Core formation and Earth's volatile accretion

4.3.1. A late volatile delivery

The experimental study of Cd, Bi, Sb and Tl behavior in a metal–silicate equilibrium and subsequent core formation modelling argues in favour of a scenario of volatile delivery in the last 10 to 20% of the main phases of Earth's accretion, in agreement with numerous other studies. A late delivery of Tl on Earth is also supported by recent study by [Fang and Liu \(2019\)](#), reporting isotopic fractionation of Tl between metal and silicate and concluding that a late delivery of Tl is needed to explain the chondritic isotopic composition of the BSE. Experimental studies on other volatile and siderophile elements show that a homogeneous accretion scenario would not reconcile the observed abundances of these elements in the BSE. In particular, for S ([Suer et al., 2017](#)), Zn ([Mahan et al., 2018b](#)) and Cu ([Mahan et al., 2018a](#)) experimental data were only reconciled with observables by volatile delivery in the last stages of Earth's accretion, a scenario also supported by [Ballhaus et al. \(2017\)](#). Amongst these references, metal–silicate diamond anvil cell experiments ([Suer et al., 2017](#); [Mahan et al., 2018a,b](#)) at conditions that are directly comparable to those of Earth's differentiation (46 to 91 GPa) lead to similar conclusions as lower pressure studies ([Ballhaus et al., 2017](#); [Mahan et al., 2017](#); [Righter et al., 2020](#)) and strengthen the relevance of the low-pressure experiments to address this issue. Experimental results on refractory siderophile elements Mo and W show that the Earth's mantle abundances are only reproduced if the S budget is accreted in the last 20% of the accretion ([Wade et al., 2012](#)). Such a scenario is also supported by experimental study on the C/S ratio of the Earth ([Li et al., 2016](#)). The existence of experimental studies focused on highly volatile, moderately volatile and refractory siderophile elements promoting heterogeneous accretion reinforces its possibility, together with non-experimental studies on a variety of isotopic and elemental measurements on elements of various volatility properties. As such, a heterogeneous accretion scenario is also supported by highly-volatile elements studies, such as noble gases ([Marty, 2012](#)). Isotopic measurements on natural samples on Pd-Ag ([Schönbächler et al., 2010](#)) also support such a scenario. Halogens natural abundances and ratios corroborates late-stage accretion of volatile rich planetesimals ([Clay et al., 2017](#)). Recent S, Se and Te measurements in chondrites and terrestrial mantle ([Braukmüller et al., 2019](#)) shows that the volatile trend in Earth and chondrites presents a “hockey-stick” pattern, forming

485 a *plateau* for the most volatile elements. A scenario of volatile delivery as 10–15 wt.% of CI-like
486 material before core formation ceased (potentially as a giant, Moon-forming impact), is proposed to
487 explain the depletion of siderophile and chalcophile volatile elements relative to the observed plateau.
488 This last stage accretion process could be associated to the formation of a S-rich and volatile-rich
489 liquid at the base of the mantle that was subsequently segregated into the core, often referred to as the
490 Hadean matte (Rubie et al., 2016; Righter et al., 2019,2020). Lastly, reported numerical simulation
491 studies investigating this late delivery process, indicate that the accreted material may originate from
492 the outer solar system (Morbidelli et al., 2012; Raymond et al., 2006) and may have been triggered by
493 the rapid migration of the giant planets (Gomes et al., 2005). This material would likely have come
494 from beyond the snow line, with a carbonaceous chondrite-like composition (Charnoz et al., 2019;
495 O'Brien et al., 2018; Schiller et al., 2018), recently supported by Mo isotopic measurements (Budde et
496 al., 2019).

497 **4.3.2. The late veneer**

498 The reconstruction of Bi partitioning by core formation models indicate that a 0.5% late veneer of CI-
499 chondrite composition is necessary to explain the Bi abundance in the Earth's mantle. However, this
500 conclusion must be considered with care as the Bi abundance in the BSE is estimated with large errors
501 (e.g. Palme and O'Neill, 2003). The late veneer has first been invoked in order to explain the relatively
502 high concentrations of highly siderophile elements (HSE) such as the platinum group elements in the
503 Earth's mantle that are impossible to reconcile with their enhanced siderophility (Holzheid et al.,
504 2000; Mann et al., 2012; O'Neill et al., 1995) as well as Pt isotopic composition (Creech et al., 2017),
505 even if some studies suggest that their siderophility could be lowered by higher PT conditions (e.g.
506 Danielson et al., 2005; Righter and Drake, 1997; Rubie et al., 2016) or by segregation in a sulphide
507 matte (Righter et al., 2018). It should be noted that HSEs present different behaviours during core
508 formation with respect to core composition and PT conditions. Recent Ru and Se isotopic
509 measurements (Fischer-Gödde et al., 2020; Varas-Reus et al., 2019) estimated a carbonaceous-
510 chondrite-like late veneer of respectively 0.3 and 0.15% of the Earth's mass. A late veneer of similar
511 composition is also supported by S, Se and Te ratios (Wang and Becker, 2013). Mass balance
512 calculations on noble metals and gas yield a smaller late veneer mass, inferior to 0.01% (Dauphas and

513 [Marty, 2002](#)). On the other hand, numerical simulation of a Grand Tack scenario linked to the
514 migration of giant planets predicts a more massive late veneer ([O'Brien et al., 2014](#)). Although there is
515 a discrepancy on the mass of the late veneer, numerous studies focusing on various cosmochemical
516 observables and using multiple methods necessitate such a late veneer to explain these observables.

517 **4.3.3. Core–mantle equilibration efficiency**

518 We show that Bi and Tl abundances in the Earth's mantle can only be explained by scenarios
519 implicating a partial equilibration process between core and mantle, also supported by other metal–
520 silicate partitioning studies (e.g. [Suer et al., 2017](#)). A low core formation efficiency has also been
521 proposed as a plausible process contributing to the observed high HSE abundances in the BSE
522 ([Arculus and Delano, 1981](#); [Jones and Drake, 1986](#); [Walker et al., 2009](#)). Geochemical models predict
523 that the degree of equilibration during core formation was 36% based on Hf–W, U–Pb and siderophile
524 elements constraints ([Rudge et al., 2010](#)). Fluid dynamics experiments by [Deguen et al. \(2014\)](#) suggest
525 that equilibration becomes less efficient as the size of the impactors increases, requiring the metal to
526 break down to fragments of 1 cm to 1 m for efficient chemical equilibration ([Rubie et al., 2003](#)). Our
527 experimental data agrees with this quantified process; however, it should be noted that recent
528 numerical simulations provide mechanisms, such as stretching of the metal, that would induce full
529 equilibration even for large differentiated planetesimals accreted to a terrestrial magma ocean ([Kendall
530 and Melosh, 2016](#); [Lherm and Deguen, 2018](#)). The conclusions of these studies based on 2D geometry
531 would favour full equilibration conditions even more strongly in the case of 3D geometry.

532 **5. Conclusions**

533 We report metal–silicate partitioning data at high pressure and high temperature for Cd, Bi, Sb and Tl
534 designed to better constrain the behaviour of MSVEs during core formation. Characterisation of such
535 partitioning helps to deconvolve the effect of differentiation from the effect of volatile-related
536 processes on the observed abundances of the studied elements in the BSE, in order to propose a
537 suitable accretion scenario of the volatile elements on Earth. Partition coefficients of Cd, Bi, Sb and Tl
538 are controlled by pressure, temperature, fO_2 and S content of the metal phase. Subsequent core
539 formation modelling shows that each studied MSVE abundance in the Earth's mantle could be

540 explained by one or several scenarios. A homogeneous accretion with full equilibration is not well
541 supported here, as it would create a deficit of Bi and Tl of roughly an order of magnitude in the
542 Earth's mantle. The most unifying scenario involves a heterogeneous scenario where the volatile
543 elements are accreted in the last 10 to 20% of the Earth's accretion, before core segregation ceased.
544 Our study also supports partial equilibration of the mantle with the core during Earth's accretion.
545 Lastly, a 0.5% late veneer of carbonaceous chondrite-like nature is required to account for the Bi
546 abundance observed in Earth's mantle.

547 **Acknowledgements**

548 We acknowledge the financial support of the UnivEarthS Labex program at Sorbonne Paris Cité
549 (ANR-10-LABX-0023 and ANR-11-IDEX-0005-02). SEM instruments are supported by IPGP
550 multidisciplinary program PARI, and by Paris-IdF region SESAME Grant No. 12015908. We thank
551 Stephan Borensztajn for support during SEM observations. We acknowledge and thank the DFG Core
552 Facility Program at Bayerisches Geoinstitut. We thank Bleuenn Guéguen for technical support during
553 LA-ICPMS measurements at IUEM, University of Brest. We also thank Nicolas Wehr for technical
554 support and advice in high-pressure laboratory of IPGP. JS thanks the financial support of the French
555 National Research Agency (ANR Project VolTerre, grant no. ANR-14-CE33-0017-01). FM
556 acknowledges funding from the European Research Council under the H2020 framework
557 program/ERC grant agreement #637503 (Pristine), and the ANR through a *chaire d'excellence*
558 Sorbonne Paris Cité.

559 **References**

- 560 Albarède, F., 2009. Volatile accretion history of the terrestrial planets and dynamic implications.
561 Nature 461, 1227–1233.
- 562 Albarède, F., Ballhaus, C., Blichert-Toft, J., Lee, C.T., Marty, B., Moynier, F., Yin, Q.Z., 2013.
563 Asteroidal impacts and the origin of terrestrial and lunar volatiles. Icarus 222, 44–52.
- 564 Arculus, R.J., Delano, J.W., 1981. Intrinsic oxygen fugacity measurements: techniques and results for
565 spinels from upper mantle peridotites and megacryst assemblages. Geochim. Cosmochim. Acta
566 45(6), 899–913.
- 567 Badro, J., Brodholt, J. P., Piet, H., Siebert, J., Ryerson, F. J., 2015. Core formation and core
568 composition from coupled geochemical and geophysical constraints. Proc. Natl. Acad. Sci.,
569 112(40):12310–12314.

- 570 Ballhaus, C., Fonseca, R.O.C., Münker, C., Rohrbach, A., Nagel, T., Speelmanns, I.M., Helmy, H.M.,
571 Zirner, A., Vogel, A.K., Heuser, A., 2017. The great sulfur depletion of Earth's mantle is not a
572 signature of mantle–core equilibration. *Contrib. to Mineral. Petrol.* 172:68.
- 573 Ballhaus, C., Laurenz, V., Münker, C., Fonseca, R.O.C., Albarède, F., Rohrbach, A., Lagos, M.,
574 Schmidt, M.W., Jochum, K.P., Stoll, B., Weis, U., Helmy, H.M., 2013. The U/Pb ratio of the
575 Earth's mantle-A signature of late volatile addition. *Earth Planet. Sci. Lett.* 362, 237–245.
- 576 Blanchard, I., Badro, J., Siebert, J., Ryerson, F.J., 2015. Composition of the core from gallium metal –
577 silicate partitioning experiments. *Earth Planet. Sci. Lett.* 427, 191–201.
- 578 Braukmüller, N., Wombacher, F., Funk, C., Münker, C., 2019. Earth's volatile element depletion
579 pattern inherited from a carbonaceous chondrite-like source. *Nat. Geosci.* 12, 564–568.
- 580 Budde, G., Burkhardt, C., Kleine, T., 2019. Molybdenum isotopic evidence for the late accretion of
581 outer Solar System material to Earth. *Nat. Astron.* 3, 736–741.
- 582 Charnoz, S., Pignatale, F.C., Hyodo, R., Mahan, B., Chaussidon, M., Siebert, J., Moynier, F., 2019.
583 Planetesimal formation in an evolving protoplanetary disk with a dead zone. *Astron. Astrophys.*
584 627, A50.
- 585 Clay, P.L., Burgess, R., Busemann, H., Ruzié-Hamilton, L., Joachim, B., Day, J.M.D., Ballentine,
586 C.J., 2017. Halogens in chondritic meteorites and terrestrial accretion. *Nature* 551, 614–618.
- 587 Corgne, A., Keshav, S., Wood, B.J., McDonough, W.F., Fei, Y., 2008. Metal-silicate partitioning and
588 constraints on core composition and oxygen fugacity during Earth accretion. *Geochim.*
589 *Cosmochim. Acta* 72, 574–589.
- 590 Creech, J.B., Baker, J.A., Handler, M.R., Lorand, J.-P., Storey, M., Wainwright, A.N., Luguét, A.,
591 Moynier, F., Bizzarro, M., 2017. Late accretion history of the terrestrial planets inferred from
592 platinum stable isotopes. *Geochemical Perspect. Lett.* 3, 94–104.
- 593 Danielson, L.R., Sharp, T.G., Hervig, R.L., 2005. Implications for core formation of the Earth from
594 high pressure-temperature Au partitioning experiments. *Lunar and Planetary Science Conference*
595 XXXVI, Lunar Planet. Inst., Houston. #1955 (abstr.).
- 596 Dauphas, N., 2017. The isotopic nature of the Earth's accreting material through time. *Nature* 541,
597 521–524.
- 598 Dauphas, N., Marty, B., 2002. Interference on the nature and the mass of Earth's late veneer from
599 noble metals and gases. *J. Geophys. Res.* 107 (E12), 5129.
- 600 Day, J.M., Brandon, A.D., Walker, R.J., 2016. Highly Siderophile Elements in Earth, Mars, the Moon,
601 and Asteroids. *Rev. Mineral. Geochem.* 81 (1), 161–238.
- 602 Deguen, R., Landeau, M., Olson, P., 2014. Turbulent metal-silicate mixing, fragmentation, and
603 equilibration in magma oceans. *Earth Planet. Sci. Lett.* 391, 274–287.
- 604 Fang, T., Liu, Y., 2019. Equilibrium thallium isotope fractionation and its constraint on Earth's late
605 veneer. *Acta Geochim.* 38 (4), 459–471.
- 606 Fischer-Gödde, M., Elfers, B.M., Münker, C., Szilas, K., Maier, W.D., Messling, N., Morishita, T.,
607 Van Kranendonk, M., Smithies H., 2020. Ruthenium isotope vestige of Earth's pre-late-veener
608 mantle preserved in Archean rocks. *Nature* 579, 240–244.
- 609 Frost, D. J., Poe, B. T., Trønnes, R. G., Liebske, C., Duba, A., Rubie, D. C., 2004. A new large-
610 volume multianvil system. *Phys. Earth Planet. Inter.*, 143(1-2):507–514.
- 611 Gomes, R., Levison, H.F., Tsiganis, K., Morbidelli, A., 2005. Origin of the cataclysmic Late Heavy
612 Bombardment period of the terrestrial planets. *Nature* 435, 466–469.

- 613 Hin, R.C., Coath, C.D., Carter, P.J., Nimmo, F., Lai, Y.J., Pogge von Strandmann, P.A.E., Willbold,
614 M., Leinhardt, Z.M., Walter, M.J., Elliott, T., 2017. Magnesium isotope evidence that accretional
615 vapour loss shapes planetary compositions. *Nature* 549, 511–527.
- 616 Holzheid, A., Sylvester, P., O'Neill, H.S.C., Rubie, D.C., Palme, H., 2000. Evidence for a late
617 chondritic veneer in the Earth's mantle from high-pressure partitioning of palladium and
618 platinum. *Nature* 406, 396–399.
- 619 Humayun, M., Clayton, R.N., 1995. Potassium isotope cosmochemistry: Genetic implications of
620 volatile element depletion. *Geochim. Cosmochim. Acta* 59, 2131–2148.
- 621 Jones, J.H., Drake, M.J., 1986. Geochemical constraints on core formation in the Earth. *Nature*,
622 322(6076), 221–228.
- 623 Kendall, J.D., Melosh, H.J., 2016. Differentiated planetesimal impacts into a terrestrial magma ocean:
624 Fate of the iron core. *Earth Planet. Sci. Lett.* 448, 24–33.
- 625 Lee, S.K., Fei, Y., Cody, G.D., Mysen, B.O., 2003. Order and disorder in sodium silicate glasses and
626 melts at 10 GPa. *Geophys. Res. Lett.* 30, 1845.
- 627 Lherm, V., Deguen, R., 2018. Small-scale Metal/Silicate Equilibration During Core Formation: The
628 Influence of Stretching Enhanced Diffusion on Mixing. *J. Geophys. Res. Solid Earth* 123,
629 10496–10516.
- 630 Li, Y., Dasgupta, R., Tsuno, K., Monteleone, B., Shimizu, N., 2016. Carbon and sulfur budget of the
631 silicate Earth explained by accretion of differentiated planetary embryos. *Nat. Geosci.* 9, 781–
632 785.
- 633 Lodders, K., 2003. Solar System Abundances and Condensation Temperatures of the Elements.
634 *Astrophys. J.* 591, 1220–1247.
- 635 Luck, J.M., Othman, D. Ben, Albarède, F., 2005. Zn and Cu isotopic variations in chondrites and iron
636 meteorites: Early solar nebula reservoirs and parent-body processes. *Geochim. Cosmochim. Acta*
637 69, 5351–5363.
- 638 Ma, Z., 2001. Thermodynamic description for concentrated metallic solutions using interaction
639 parameters. *Metall. Mater. Trans. B* 32, 87–103.
- 640 Mahan, B., Siebert, J., Blanchard, I., Badro, J., Kubik, E., Sossi, P., Moynier, F., 2018a. Investigating
641 Earth's Formation History Through Copper and Sulfur Metal-Silicate Partitioning During Core-
642 Mantle Differentiation. *J. Geophys. Res. Solid Earth* 123, 8349–8363.
- 643 Mahan, B., Siebert, J., Blanchard, I., Borensztajn, S., Badro, J., Moynier, F., 2018b. Constraining
644 compositional proxies for Earth's accretion and core formation through high pressure and high
645 temperature Zn and S metal-silicate partitioning. *Geochim. Cosmochim. Acta* 235, 21–40.
- 646 Mahan, B., Siebert, J., Pringle, E.A., Moynier, F., 2017. Elemental partitioning and isotopic
647 fractionation of Zn between metal and silicate and geochemical estimation of the S content of the
648 Earth's core. *Geochim. Cosmochim. Acta* 196, 252–270.
- 649 Mann, U., Frost, D.J., Rubie, D.C., Becker, H., Audétat, A., 2012. Partitioning of Ru, Rh, Pd, Re, Ir
650 and Pt between liquid metal and silicate at high pressures and high temperatures - Implications
651 for the origin of highly siderophile. *Geochim. Cosmochim. Acta* 84, 593–613.
- 652 Marty, B., 2012. The origins and concentrations of water, carbon, nitrogen and noble gases on Earth.
653 *Earth Planet. Sci. Lett.* 313–314, 56–66.
- 654 McDonough, W.F., 2003. Compositional Model for the Earth's Core. In *Treatise On Geochemistry*,
655 vol. 2 (ed. R. W. Carlson). Elsevier-Pergamon. Oxford, pp. 547–568.
- 656 Médard, E., Schmidt, M.W., Wälle, M., Keller, N.S., Günther, D., 2015. Platinum partitioning

- 657 between metal and silicate melts: Core formation, late veneer and the nanonuggets issue.
658 *Geochim. Cosmochim. Acta* 162, 183–201.
- 659 Morard, G., Sanloup, C., Fiquet, G., Mezouar, M., Rey, N., Poloni, R., Beck, P., 2007. Structure of
660 eutectic Fe-FeS melts to pressures up to 17 GPa: Implications for planetary cores. *Earth Planet.*
661 *Sci. Lett.* 263, 128–139.
- 662 Morbidelli, A., Lunine, J.I., O'Brien, D.P., Raymond, S.N., Walsh, K.J., 2012. Building Terrestrial
663 Planets. *Annu. Rev. Earth Planet. Sci.* 40, 251–275.
- 664 Norris, C.A., Wood, B.J., 2017. Earth's volatile contents established by melting and vaporization.
665 *Nature* 549, 507–510.
- 666 O'Brien, D.P., Walsh, K.J., Morbidelli, A., Raymond, S.N., Mandell, A.M., 2014. Water delivery and
667 giant impacts in the 'Grand Tack' scenario. *Icarus* 239, 74–84.
- 668 O'Brien, D.P., Izidoro, A., Jacobson, S.A., Raymond, S.N., Rubie, D.C., 2018. The Delivery of Water
669 During Terrestrial Planet Formation. *Space Sci. Rev.* 214:47.
- 670 O'Neill, H.S.C., Dingwell, D.B., Borisov, A., Spettel, B., Palme, H., 1995. Experimental
671 petrochemistry of some highly siderophile elements at high temperatures, and some implications
672 for core formation and the mantle's early history. *Chem. Geol.* 120, 255–273.
- 673 O'Neill, H.S.C., 1991. The origin of the moon and the early history of the earth-A chemical model.
674 Part 1: The moon. *Geochim. Cosmochim. Acta* 55, 1135–1157.
- 675 O'Neill, H.S.C., Palme, H., 2008. Collisional erosion and the non-chondritic composition of the
676 terrestrial planets. *Philos. Trans. R. Soc. A Math. Phys. Eng. Sci.* 366, 4205–4238.
- 677 Palme, H., O'Neill, H. S. C., 2003. *Cosmochemical Estimates of Mantle Composition*, volume 2.
678 Elsevier Ltd., first edition.
- 679 Pringle, E.A., Moynier, F., 2017. Rubidium isotopic composition of the Earth, meteorites, and the
680 Moon: Evidence for the origin of volatile loss during planetary accretion. *Earth Planet. Sci. Lett.*
681 473, 62–70.
- 682 Pringle, E.A., Moynier, F., Beck, P., Paniello, R., Hezel, D.C., 2017. The origin of volatile element
683 depletion in early solar system material: Clues from Zn isotopes in chondrules. *Earth Planet. Sci.*
684 *Lett.* 468, 62–71.
- 685 Pringle, E.A., Moynier, F., Savage, P.S., Badro, J., Barrat, J.-A., 2014. Silicon isotopes in angrites and
686 volatile loss in planetesimals. *Proc. Natl. Acad. Sci.* 111, 17029–17032.
- 687 Raymond, S.N., Quinn, T., Lunine, J.I., 2006. High-resolution simulations of the final assembly of
688 Earth-like planets I. Terrestrial accretion and dynamics. *Icarus* 183, 265–282.
- 689 Righter, K., Humayun, M., Campbell, A.J., Danielson, L., Hill, D., Drake, M.J., 2009. Experimental
690 studies of metal–silicate partitioning of Sb: Implications for the terrestrial and lunar mantles.
691 *Geochim. Cosmochim. Acta* 73, 1487–1504.
- 692 Righter, K., Drake, M.J., 1997. Metal–silicate equilibrium in a homogeneously accreting earth: new
693 results for Re. *Earth Planet. Sci. Lett.* 146, 541–553.
- 694 Righter, K., Pando, K., Marin, N., Ross, D.K., Righter, M., Danielson, L., Lapen, T.J., Lee, C., 2017a.
695 Volatile element signatures in the mantles of Earth, Moon, and Mars: Core formation fingerprints
696 from Bi, Cd, In, and Sn. *Meteorit. Planet. Sci.* 22, 1–22.
- 697 Righter, K., Nickodem, K., Pando, K., Danielson, L., Boujibar, A., Righter, M., Lapen, T.J., 2017b.
698 Distribution of Sb, As, Ge, and In between metal and silicate during accretion and core formation
699 in the Earth. *Geochim. Cosmochim. Acta* 198, 1–16.

- 700 Righter, K., Pando, K., Humayun, M., Waesermann, N., Yang, S., Boujibar, A., Danielson, L. R.,
701 2018. Effect of silicon on activity coefficients of siderophile elements (Au, Pd, Pt, P, Ga, Cu, Zn,
702 and Pb) in liquid Fe: Roles of core formation, late sulfide matte, and late veneer in shaping
703 terrestrial mantle geochemistry. *Geochim. Cosmochim. Acta*, 232:101–123.
- 704 Righter, K., Pando, K., Ross, D.K., Righter, M., Lapen, T.J., 2019. Effect of silicon on activity
705 coefficients of Bi, Cd, Sn, and Ag in liquid Fe-Si, and implications for differentiation and core
706 formation. *Meteorit. Planet. Sci.* 54, 1379–194.
- 707 Righter, K., Schönbacher, M., Pando, K., Rowland II, R., Righter, M., Lapen, T., 2020. Ag isotopic
708 and chalcophile element evolution of the terrestrial and martian mantles during accretion: New
709 constraints from Bi and Ag metal-silicate partitioning. *Earth Planet. Sci. Lett.* 552, 116590.
- 710 Rubie, D. C., 1999. Characterizing the sample environment in multianvil high-pressure experiments.
711 *Phase Transit.*, 68(3):431–451.
- 712 Rubie, D.C., Melosh, H.J., Reid, J.E., Liebske, C. and Righter, K., 2003. Mechanisms of metal–
713 silicate equilibration in the terrestrial magma ocean. *Earth Planet. Sci. Lett.* 205(3-4), 239–255.
- 714 Rubie, D.C., Frost, D.J., Mann, U., Asahara, Y., Nimmo, F., Tsuno, K., Kegler, P., Holzheid, A.,
715 Palme, H., 2011. Heterogeneous accretion, composition and core-mantle differentiation of the
716 Earth. *Earth Planet. Sci. Lett.* 301, 31–42.
- 717 Rubie, D.C., Jacobson, S.A., Morbidelli, A., O’Brien, D.P., Young, E.D., de Vries, J., Nimmo, F.,
718 Palme, H., Frost, D.J., 2015. Accretion and differentiation of the terrestrial planets with
719 implications for the compositions of early-formed Solar System bodies and accretion of water.
720 *Icarus* 248, 89–108.
- 721 Rubie, D.C., Laurenz, V., Jacobson, S.A., Morbidelli, A., Palme, H., Vogel, A.K., Frost, D.J., 2016.
722 Highly siderophile elements were stripped from Earth’s mantle by iron sulphide segregation.
723 *Science* 353 1141–1144.
- 724 Rudge, J.F., Kleine, T., Bourdon, B., 2010. Broad bounds on Earths accretion and core formation
725 constrained by geochemical models. *Nat. Geosci.* 3, 439–443.
- 726 Sanloup, C., van Westrenen, W., Dasgupta, R., Maynard-Casely, H., Perillat, J.-P., 2011.
727 Compressibility change in iron-rich melt and implications for core formation models. *Earth*
728 *Planet. Sci. Lett.* 306, 118–122.
- 729 Savage, P.S., Moynier, F., Chen, H., Shofner, G., Siebert, J., Badro, J., Puchtel, I.S., 2015. Copper
730 isotope evidence for large-scale sulphide fractionation during Earth’s differentiation.
731 *Geochemical Perspect. Lett.* 1, 53–64.
- 732 Schiller, M., Bizzarro, M., Fernandes, V.A., 2018. Isotopic evolution of the protoplanetary disk and
733 the building blocks of Earth and the Moon. *Nature* 555, 501–510.
- 734 Schonbacher, M., Carlson, R.W., Horan, M.F., Mock, T.D., Hauri, E.H., 2010. Heterogeneous
735 Accretion and the Moderately Volatile Element Budget of Earth. *Science* 328, 884–887.
- 736 Siebert, J., Malavergne, V., Guyot, F., Combes, R., Martinez, I., 2004. The behaviour of sulphur in
737 metal–silicate core segregation experiments under reducing conditions. *Phys. Earth Planet. Inter.*
738 143–144, 433–443.
- 739 Siebert, J., Corgne, A., Ryerson, F.J., 2011. Systematics of metal-silicate partitioning for many
740 siderophile elements applied to Earth’s core formation. *Geochim. Cosmochim. Acta* 75, 1451–
741 1489.
- 742 Siebert, J., Sossi, P.A., Blanchard, I., Mahan, B., Badro, J., Moynier, F., 2018. Chondritic Mn/Na ratio
743 and limited post-nebular volatile loss of the Earth. *Earth Planet. Sci. Lett.* 485, 130–139.
- 744 Sossi, P.A., Nebel, O., O’Neill, H.S.C., Moynier, F., 2017. Zinc isotope composition of the Earth and

- 745 its behaviour during planetary accretion. *Chem. Geol.* 477, 73–84.
- 746 Steenstra, E.S., Lin, Y., Dankers, D., Rai, N., Berndt, J., Matveev, S., van Westrenen, W., 2017. The
747 lunar core can be a major reservoir for volatile elements S, Se, Te and Sb. *Sci. Rep.* 7:14552.
- 748 Steenstra, E.S., Dankers, D., Berndt, J., Klemme, S., Matveev, S., van Westrenen, W., 2019.
749 Significant depletion of volatile elements in the mantle of asteroid Vesta due to core formation.
750 *Icarus* 317, 669–681.
- 751 Steenstra, E.S., Seegers, A.X., Putter, R., Berndt, J., Klemme, S., Matveev, S., Bullock, E.S., 2020a.
752 Metal-silicate partitioning systematics of siderophile elements at reducing conditions: A new
753 experimental database. *Icarus* 335, 113391.
- 754 Steenstra, E.S., Berndt, J., Klemme, S., Fei, Y., van Westrenen, W., 2020b. A possible high-
755 temperature origin of the Moon and its geochemical consequences. *Earth Planet. Sci. Lett.* 538,
756 116222.
- 757 Suer, T.A., Siebert, J., Remusat, L., Menguy, N., Fiquet, G., 2017. A sulfur-poor terrestrial core
758 inferred from metal–silicate partitioning experiments. *Earth Planet. Sci. Lett.* 469, 84–97.
- 759 Thibault, Y., Walter, M.J., 1995. The influence of pressure and temperature on the metal-silicate
760 partition coefficients of nickel and cobalt in a model CI chondrite and implications for metal
761 segregation in a deep magma ocean. *Geochim. Cosmochim. Acta* 59, 991–1002.
- 762 Tuller-Ross, B., Marty, B., Chen, H., Kelley, K.A., Lee, H., Wang, K., 2019. Potassium isotope
763 systematics of oceanic basalts. *Geochim. Cosmochim. Acta* 259, 144–154.
- 764 Van Achterbergh, E., Ryan, C.G., Griffin, W.L., 1999. GLITTER: on-line interactive data reduction
765 for the laser ablation inductively coupled plasma mass spectrometry microprobe. In: Ninth
766 Annual VM Goldschmidt Conference. August 1999.
- 767 Varas-Reus, M.I., König, S., Yierpan, A., Lorand, J.P., Schoenberg, R., 2019. Selenium isotopes as
768 tracers of a late volatile contribution to Earth from the outer Solar System. *Nat. Geosci.* 12, 779–
769 782.
- 770 Vogel, A.K., Jennings, E.S., Laurenz, V., Rubie, D.C., Frost, D.J., 2018. The dependence of metal-
771 silicate partitioning of moderately volatile elements on oxygen fugacity and Si contents of Fe
772 metal: Implications for their valence states in silicate liquids. *Geochim. Cosmochim. Acta* 237,
773 275–293.
- 774 Wade, J., Wood, B.J., 2005. Core formation and the oxidation state of the Earth. *Earth Planet. Sci.*
775 *Lett.* 236, 78–95.
- 776 Wade, J., Wood, B.J., Tuff, J., 2012. Metal–silicate partitioning of Mo and W at high pressures and
777 temperatures: Evidence for late accretion of sulphur to the Earth. *Geochim. Cosmochim. Acta*
778 85, 58–74.
- 779 Walker, R.J., 2009. Highly siderophile elements in the Earth, Moon and Mars: update and implications
780 for planetary accretion and differentiation. *Geochem.*, 69(2), 101–125.
- 781 Wang, K., Jacobsen, S.B., 2016. Potassium isotopic evidence for a high-energy giant impact origin of
782 the Moon. *Nature* 538, 487–490.
- 783 Wang, Z., Becker, H., 2013. Ratios of S, Se and Te in the silicate Earth require a volatile-rich late
784 veneer. *Nature* 499, 328–332.
- 785 Wang, Z., Laurenz, V., Petitgirard, S., Becker, H., 2016. Earth’s moderately volatile element
786 composition may not be chondritic: Evidence from In, Cd and Zn. *Earth Planet. Sci. Lett.* 435,
787 136–146.
- 788 Wasson, J.T., Kallemeyn, G.W., Runcorn, S.K., Turner, G., Woolfson, M.M., 1988. Compositions of

- 789 chondrites. *Philos. Trans. R. Soc. London. Ser. A, Math. Phys. Sci.* 325, 535–544.
- 790 Wood, B.J., Nielsen, S.G., Rehkämper, M., Halliday, A.N., 2008. The effects of core formation on the
791 Pb- and Tl- isotopic composition of the silicate Earth. *Earth Planet. Sci. Lett.* 269, 326–336.
- 792 Wood, B.J., Halliday, A.N., 2010. The lead isotopic age of the Earth can be explained by core
793 formation alone. *Nature* 465, 767–770.
- 794 Wood, B.J., Kiseeva, E.S., Mirolo, F.J., 2014. Accretion and core formation: The effects of sulfur on
795 metal–silicate partition coefficients. *Geochim. Cosmochim. Acta* 145, 248–267.
- 796 Wood, B.J., Smythe, D.J., Harrison, T., 2019. The condensation temperatures of the elements: A
797 reappraisal. *Am. Mineral.* 104, 844–856.
- 798 Young, E.D., Shahar, A., Nimmo, F., Schlichting, H.E., Schauble, E.A., Tang, H., Labidi, J., 2019.
799 Near-equilibrium isotope fractionation during planetesimal evaporation. *Icarus* 323, 1–15.
- 800

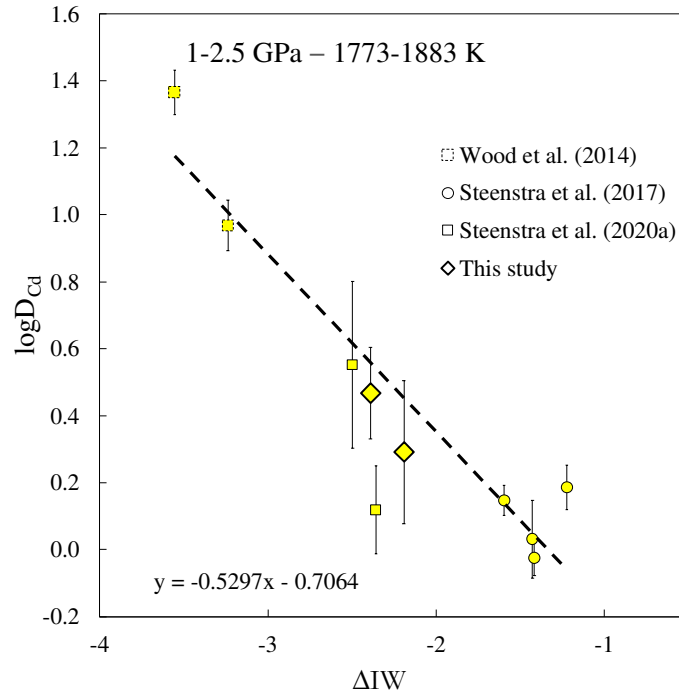


Figure 1: Partition coefficient $\log D_{Cd}$ as a function of oxygen fugacity ΔIW calculated relatively to iron-wüstite (Equation 1) for all experiments between 1 and 2.5 GPa and 1773–1883 K of this study and data compiled from the literature (Steenstra et al., 2017,2020a; Wood et al., 2014). Errors correspond to 1 standard deviation (σ) and were propagated from EPMA and LA-ICPMS measurements of this study and from the literature. The variation in partition coefficient over a significant interval of fO_2 allows accurate determination of the valence state of Cd. In fact, it can be demonstrated that $\log D_{Sn}$ is a function of $\frac{n}{4} \log fO_2$ (Siebert et al., 2011). With the slope of the regression line shown on this figure equal to 0.5, we demonstrate that Cd has a valence of 2+ over a range of more than 2 log units.

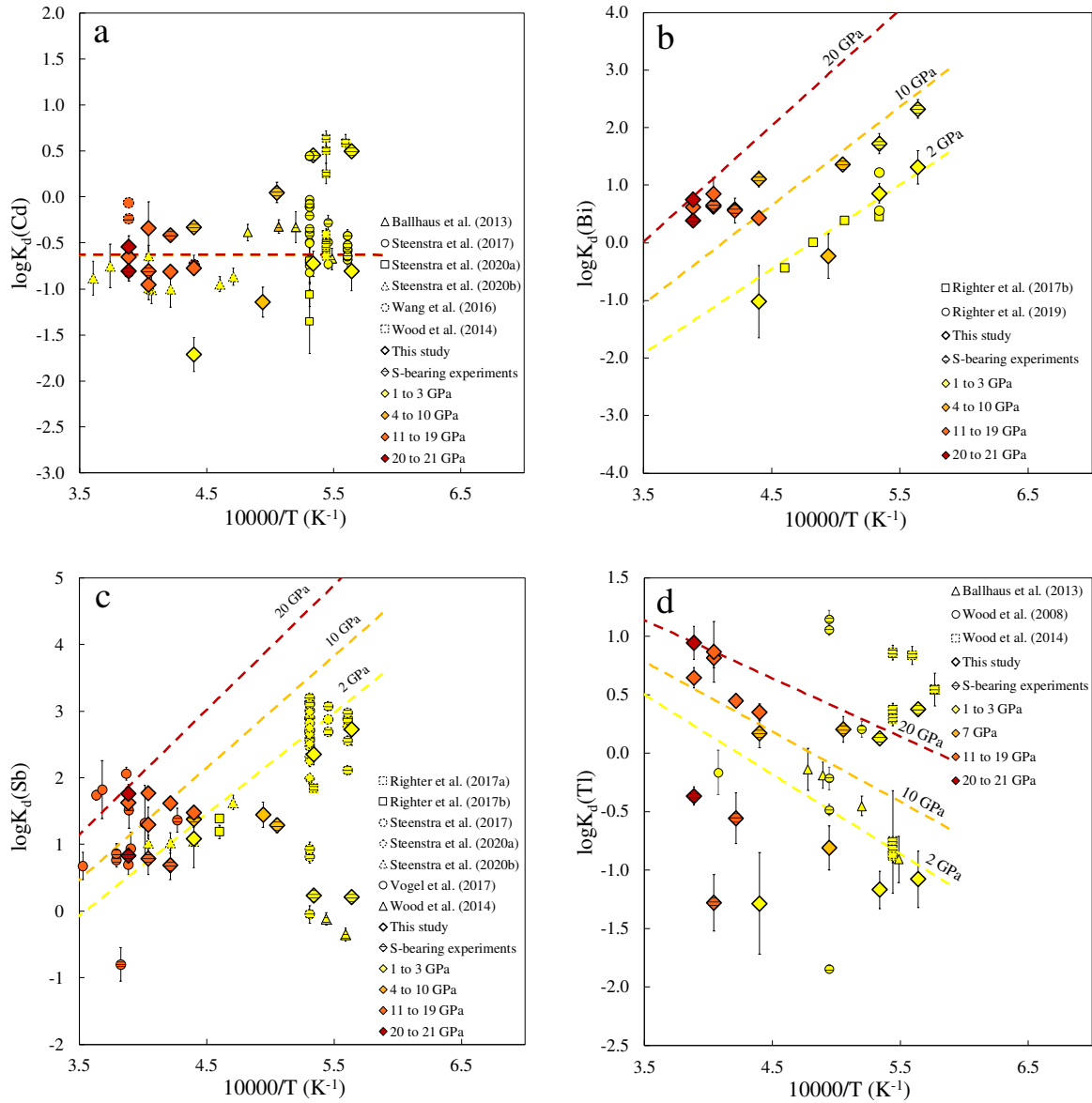


Figure 2: Exchange coefficient $\log K_d$ as a function of reciprocal temperature for Cd, Bi, Sb and Tl and for all experiments of this study and literature data. Errors are 1 standard deviation (σ) propagated from EPMA and LA-ICPMS measurements of this study and from the literature. Experiments holding more than 1 mol% of S in the metal part are differentiated by a horizontal lines pattern. All experiments are color-coded according to their run pressure: 1–3 GPa in yellow, 4–10 GPa in orange, 10–19 GPa in light red, >19 GPa in dark red. Multilinear regression fits are also displayed at IW-2 in the following conditions: 2 GPa, 10 GPa, and 20 GPa with no S in the metal.

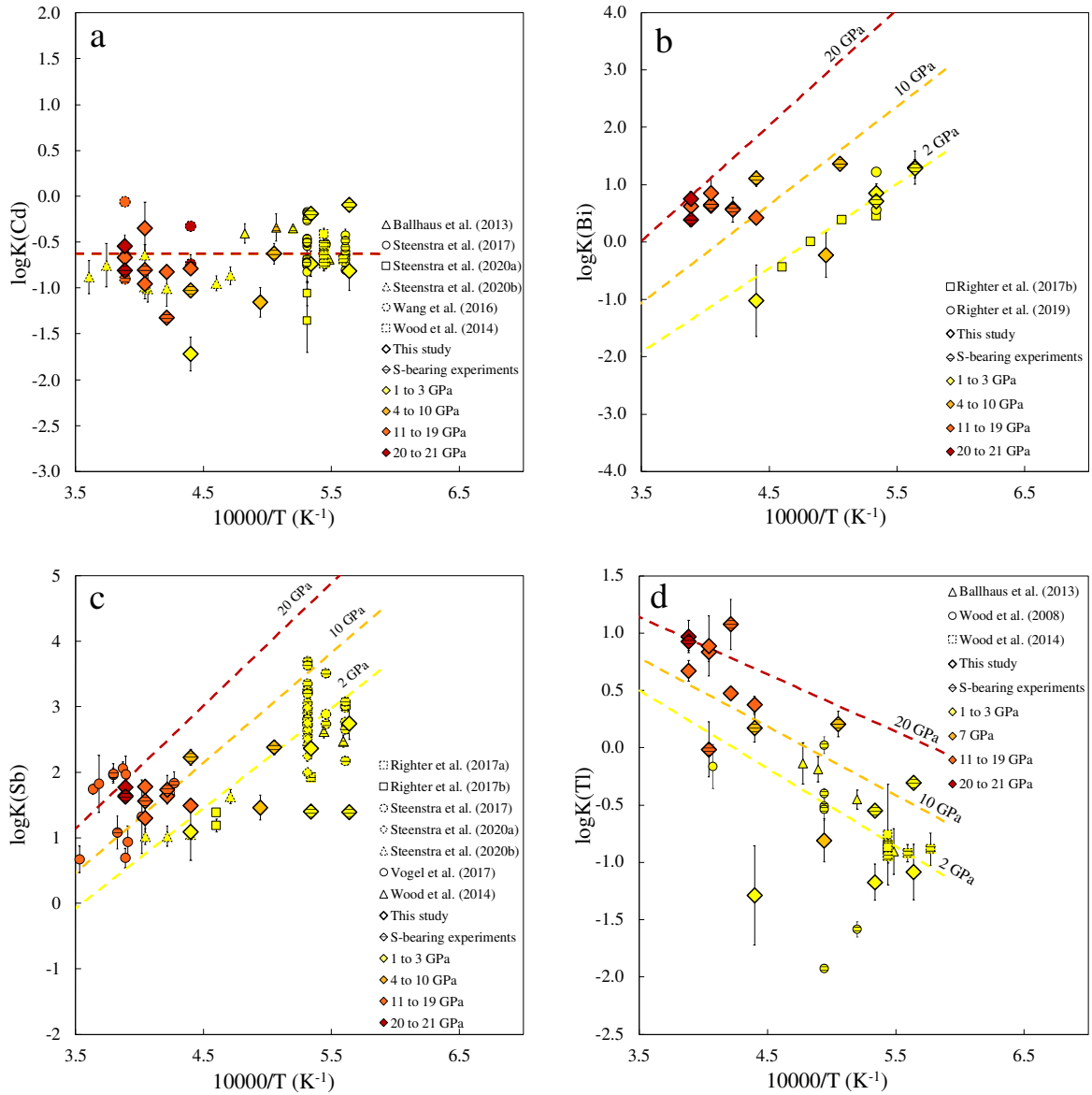


Figure 3: $\log K$ determined experimentally as a function of reciprocal temperature for Cd, Bi, Sb and Tl and for all experiments of this study and literature data. Errors correspond to 1 standard deviation (σ) and were propagated from EPMA and LA-ICPMS measurements of this study and from the literature. Experiments holding more than 1 mol% of S in the metal are differentiated by a horizontal lines pattern. All experiments are color-coded according to their run pressure: 1–3 GPa in yellow, 4–10 GPa in orange, 11–19 GPa in light red, >19 GPa in dark red. Multilinear regression fits are also displayed at IW-2 in the following conditions: 2 GPa, 10 GPa, and 20 GPa with no S in the metal. $\log K$ being defined as $a + b \cdot \frac{1}{T} + c \cdot \frac{P}{T}$, this figure displays the effect of pressure and temperature alone on M partitioning between metal and silicate, meaning that the partitioning is corrected for the effect of S.

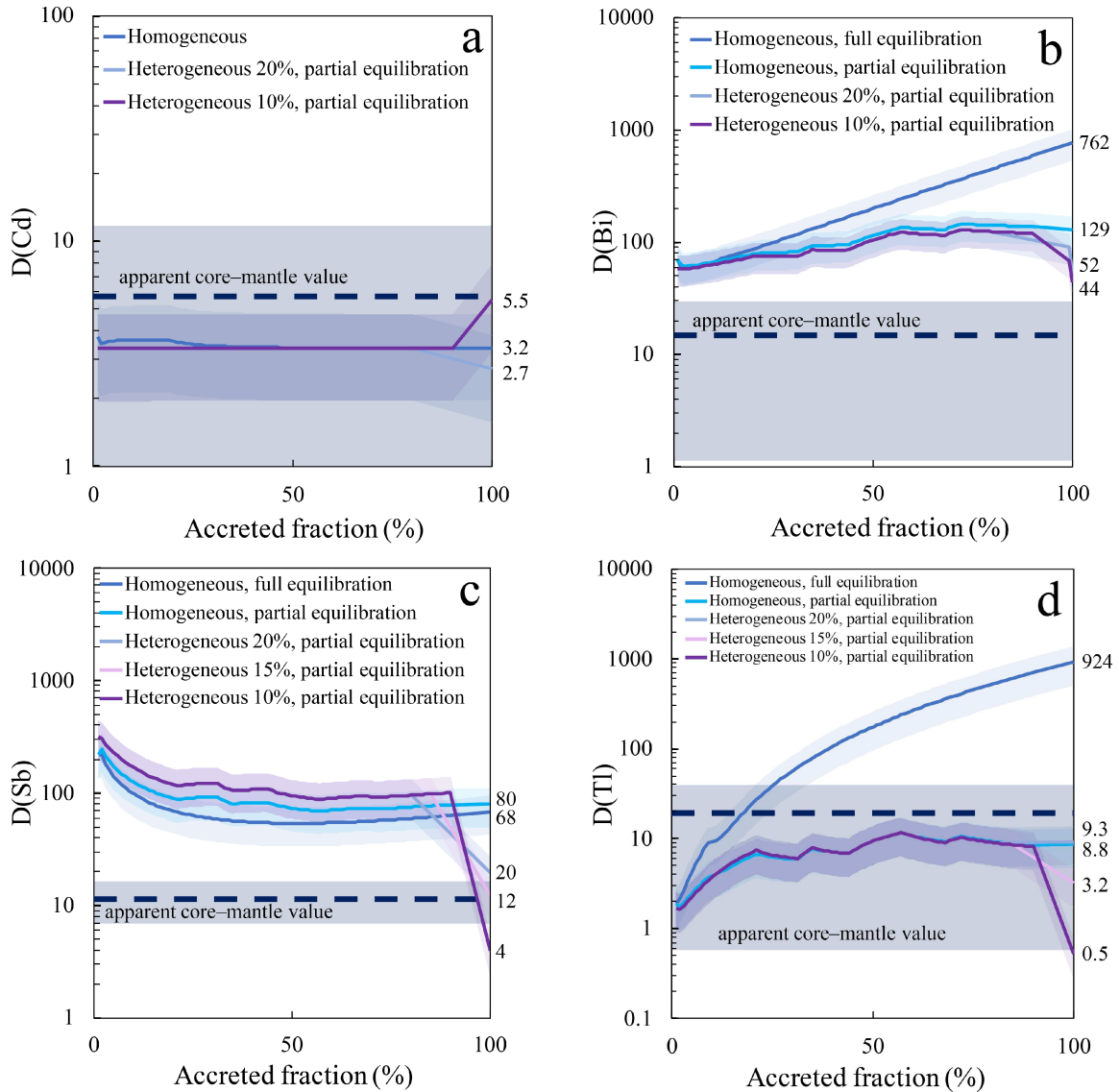


Figure 4: Evolution of D_M during Earth's accretion computed for Cd, Bi, Sb and Tl from core formation models with full and partial equilibration, and homogeneous and heterogeneous scenarios. Apparent core–mantle values are represented as a dark blue zone with its central value as a dashed line. Errors of models are propagated from error percentages on the computed regression coefficients. For all partial equilibration models, ϵ was computed with $k=0.5$. In calculations involving a partial equilibration, D_M is sensitive to the size of the accreted embryos which is why we observe variations on the curves at stages where there is a change of the size of accreted bodies. All models were computed at constant fO_2 of IW-2.3 and with 1.9 wt.% S in the core of the Earth and differentiated embryos. **a.** With no pressure and temperature effect, D_{Cd} evolution is the same for homogeneous accretion scenario, whether partial or full equilibration is modeled, with a final partitioning of 3.2 ± 1.4 . The apparent core–mantle value ranges from 0 to 11.5, with all the models computed here being a match to this estimation. However, a heterogeneous scenario with an accretion of the volatiles in the last 10% yields a final D_{Cd} of 5.5 ± 2.3 which is closer to the central estimated value. On the contrary, with a scenario of volatile delivery in the last 20%, the final D_{Cd} is 2.7 ± 1.1 sits further from the central value, due to a different effect of S in the last accreted embryo. **b.** The estimated D_{Bi} of the Earth ranges from 1.3 to 28.9. The reconstructed partitioning for a scenario of full equilibration with compositionally homogeneous accretion is one order of magnitude higher than the observed value, with a final D_{Bi} of 762 ± 225 , and is still significantly higher with a homogeneous scenario with partial equilibration (final $D_{Bi} = 129 \pm 38$). Two scenarios consider an accretion of the volatiles in the last 10 and 20% of the accretion including a 0.5 wt.% late veneer of CI chondrite-like material and present final D_{Bi} of 44 ± 13 and 52 ± 15 respectively. **c.** In the case of Sb, the scenario of partial equilibration with homogeneous accretion presents a higher final partitioning (80 ± 29) than the full equilibration with homogeneous accretion scenario (68 ± 25) because of the strong negative effect of S which is undermined by a less efficient equilibration. These two scenarios are higher than the apparent core–mantle D_{Sb} which ranges from 7.2 to 15.9. Three heterogeneous scenarios were modeled with an accretion of the volatile elements in the last 10, 15 and 20% of the Earth's formation and yield final partitioning of respectively 4 ± 1 , 12 ± 4 and 20 ± 7 , the 15% late accretion being the best match to the central observed value. **d.** The apparent core–mantle D_{Tl} value ranges from 0.6 to 37.8. The homogeneous model with full equilibration yields a final D_{Tl} of 924 ± 414 , which is too high to reconcile the experimental data with the observed abundances through this scenario. Using a partial equilibration model allows to match the observed partitioning with the following final D_{Tl} : 8.8 ± 4 for a homogeneous accretion, 3.2 ± 1 for a delivery of

volatiles in the last 15% of Earth's accretion and 9.3 ± 4 for a delivery in the last 20%. A scenario of accretion of the volatiles in the last 10% of the Earth's accretion presents a final D_{71} within error of the target value (0.5 ± 0.2).

Table 1: Starting material compositions (*wt.%*).

Starting material	Silicate phase	Metallic phase			
	MORB	Fe	FeS	Dopants	
				Sn	Cu, Tl, In, Cd, Bi, Sb
A	70%	30%		2%	1% of each
B	70%	13.5%	16.5%	2%	1% of each

Table 2: Main parameters of all experiments, average major and trace element compositions of metal and silicate phases by EPMA and LA-ICPMS. Errors correspond to 1 standard deviation σ .

Experiment	E317	E342	E345	H4735	H4950	H4951	H4952	E396	E397
Starting material	A	A	A	B	A	A	B	B	B
Pressure (GPa)	2	2	2	10	12	14	12	2	2
Temperature (K)	1873	1773	2273	2275	2273	2373	2373	1873	1773
Duration (min)	5	15	1	5	5	2	2	5	15
Pressure media	Talc-pyrex	Talc-pyrex	BaCO ₃	MgO+Cr ₂ O ₃	Talc-pyrex	Talc-pyrex			
Capsule	MgO	MgO	MgO	MgO SC	MgO SC	MgO SC	MgO SC	MgO	MgO
Silicate composition (oxide wt.%)									
n	21	18	25	30	13	14	10	13	29
SiO ₂	40.05 ± 0.46	41.14 ± 0.26	30.15 ± 0.51	37.66 ± 0.20	38.57 ± 0.16	37.99 ± 0.32	36.54 ± 0.54	41.44 ± 1.43	39.79 ± 0.19
Al ₂ O ₃	10.66 ± 1.12	10.00 ± 1.23	8.26 ± 0.15	9.24 ± 0.15	9.10 ± 0.25	10.16 ± 0.17	8.27 ± 0.13	10.06 ± 0.76	12.56 ± 0.31
CaO	8.54 ± 0.96	7.94 ± 1.05	7.60 ± 0.15	8.60 ± 0.18	9.22 ± 0.19	9.26 ± 0.23	8.66 ± 0.28	7.65 ± 0.70	10.15 ± 0.31
MgO	29.35 ± 2.56	27.88 ± 2.97	28.59 ± 0.84	34.31 ± 0.31	35.71 ± 0.36	34.74 ± 0.42	37.06 ± 0.60	24.58 ± 1.02	20.12 ± 0.75
FeO	8.26 ± 0.25	10.11 ± 0.12	11.66 ± 0.24	7.09 ± 0.10	5.67 ± 0.13	5.95 ± 0.09	7.41 ± 0.09	10.64 ± 0.86	13.39 ± 0.10
Na ₂ O	1.85 ± 0.22	1.53 ± 0.21	1.15 ± 0.03	0.78 ± 0.02	1.18 ± 0.05	1.22 ± 0.04	1.01 ± 0.04	2.06 ± 0.13	1.99 ± 0.05
TiO ₂	0.71 ± 0.08	0.68 ± 0.09	0.46 ± 0.01	0.72 ± 0.03	0.70 ± 0.03	0.73 ± 0.03	0.71 ± 0.03	0.69 ± 0.07	0.88 ± 0.03
K ₂ O	0.20 ± 0.02	0.15 ± 0.02	0.15 ± 0.003	0.16 ± 0.01	0.13 ± 0.01	0.14 ± 0.01	0.09 ± 0.01	0.20 ± 0.02	0.17 ± 0.003
P ₂ O ₅	0.01 ± 0.001	0.02 ± 0.002	0.06 ± 0.003	0.06 ± 0.003	0.01 ± 0.000	0.01 ± 0.001	0.07 ± 0.003	0.07 ± 0.01	0.09 ± 0.001
SO ₂	0.01 ± 0.001	0.01 ± 0.001	0.05 ± 0.003	0.12 ± 0.01	0.01 ± 0.001	0.01 ± 0.001	0.55 ± 0.04	0.18 ± 0.02	0.24 ± 0.01
SrO								0.07 ± 0.01	0.08 ± 0.003
CdO								0.09 ± 0.01	0.11 ± 0.003
Bi ₂ O ₃								0.002 ± 0.001	0.001 ± 0.000
Sb ₂ O ₃								0.10 ± 0.01	0.14 ± 0.005
Tl ₂ O ₃								0.22 ± 0.02	0.24 ± 0.01
Total	99.99 ± 0.31	99.74 ± 0.28	88.61 ± 0.51	99.30 ± 0.17	100.89 ± 0.12	100.76 ± 0.13	101.30 ± 0.26	98.18 ± 0.36	100.08 ± 0.50
Sn (ppm)	268 ± 80	300 ± 136	1146 ± 226	1008 ± 100	222 ± 19	188 ± 26	2106 ± 146		
Cd (ppm)	982 ± 292	1677 ± 736	1774 ± 545	2528 ± 57	2621 ± 80	2458 ± 113	1628 ± 75		
Bi (ppm)	4 ± 1	4 ± 3	140 ± 199	29 ± 9	59 ± 5	46 ± 6	114 ± 54		
Sb (ppm)	2 ± 1	1 ± 1	81 ± 81	30 ± 8	13 ± 2	10 ± 1	108 ± 55		
Tl (ppm)	2282 ± 651	3600 ± 1527	2401 ± 708	702 ± 72	1354 ± 141	805 ± 90	938 ± 88		
Metal composition (wt.%)									
n	31	27	25	28	14	11	15	12	14
Fe	87.58 ± 0.26	86.76 ± 0.64	89.51 ± 0.16	64.91 ± 0.35	80.66 ± 0.61	80.73 ± 0.72	60.63 ± 0.60	62.80 ± 1.26	63.33 ± 0.55
Sn	3.82 ± 0.05	3.86 ± 0.03	3.43 ± 0.06	5.29 ± 0.06	5.08 ± 0.11	4.55 ± 0.05	5.21 ± 0.07	5.33 ± 0.21	5.20 ± 0.13
P	0.08 ± 0.004	0.09 ± 0.004	0.001 ± 0.000	0.01 ± 0.001	0.09 ± 0.004	0.11 ± 0.004	0.01 ± 0.002	0.02 ± 0.004	0.02 ± 0.002
S	0.24 ± 0.01	0.24 ± 0.01	0.10 ± 0.01	16.15 ± 0.14	0.26 ± 0.01	0.29 ± 0.02	19.98 ± 0.26	10.31 ± 0.40	11.08 ± 0.23
Si	0.02 ± 0.002	0.01 ± 0.002	0.01 ± 0.001	0.01 ± 0.002	0.04 ± 0.01	0.02 ± 0.004	0.02 ± 0.001	0.01 ± 0.004	0.03 ± 0.03
O	0.01 ± 0.01	0.16 ± 0.04	N.D.	1.32 ± 0.13	0.19 ± 0.03	0.17 ± 0.05	1.41 ± 0.27	0.42 ± 0.07	0.55 ± 0.05
Ti	N.D.	0.004 ± 0.001	0.003 ± 0.001	N.D.	0.01 ± 0.002	N.D.	N.D.	0.002 ± 0.001	0.003 ± 0.001
Mg	0.14 ± 0.002	0.14 ± 0.002	0.15 ± 0.004	0.10 ± 0.00	0.13 ± 0.004	0.13 ± 0.004	0.08 ± 0.001	0.09 ± 0.01	0.09 ± 0.01
Cd	0.26 ± 0.03	0.29 ± 0.06	0.03 ± 0.01	1.42 ± 0.05	0.82 ± 0.07	0.67 ± 0.04	0.66 ± 0.05	1.77 ± 0.14	1.80 ± 0.12
Bi	0.15 ± 0.03	0.33 ± 0.08	0.04 ± 0.01	1.54 ± 0.17	1.38 ± 0.09	1.42 ± 0.07	1.45 ± 0.25	2.08 ± 0.17	2.52 ± 0.25
Sb	2.60 ± 0.03	2.71 ± 0.03	3.10 ± 0.07	3.02 ± 0.05	3.54 ± 0.07	3.37 ± 0.05	1.85 ± 0.02	2.94 ± 0.17	2.82 ± 0.13
Tl	0.05 ± 0.01	0.09 ± 0.02	0.04 ± 0.01	0.36 ± 0.02	1.18 ± 0.09	0.87 ± 0.07	0.08 ± 0.04	0.39 ± 0.08	0.69 ± 0.11
Total	98.74 ± 0.22	99.10 ± 0.55	97.71 ± 0.15	98.25 ± 0.26	98.08 ± 0.50	98.24 ± 0.66	97.26 ± 0.18	92.68 ± 0.49	94.06 ± 0.17
D _{Cd}	2.9 ± 0.9	2.0 ± 1.0	0.2 ± 0.1	5.7 ± 0.3	3.8 ± 0.4	3.3 ± 0.3	4.2 ± 0.4	21.4 ± 2.5	18.8 ± 1.3
logK ^{D_{Cd}}	-0.73 ± 0.14	-0.80 ± 0.21	-1.72 ± 0.18	-0.33 ± 0.02	-0.77 ± 0.04	-0.81 ± 0.03	-0.41 ± 0.04	0.45 ± 0.06	0.49 ± 0.03
D _{Bi}	450 ± 178	907 ± 606	3 ± 4	537 ± 170	287 ± 29	374 ± 55	131 ± 65	1096 ± 428	3123 ± 1155
logK ^{D_{Bi}}	0.86 ± 0.17	1.31 ± 0.29	-1.02 ± 0.63	1.11 ± 0.14	0.43 ± 0.05	0.58 ± 0.06	0.56 ± 0.22	1.72 ± 0.17	2.32 ± 0.16
D _{Sb}	13981 ± 5108	23454 ± 13100	386 ± 386	1004 ± 281	3211 ± 519	4097 ± 478	175 ± 88	35 ± 4	24 ± 1
logK ^{D_{Sb}}	2.35 ± 0.16	2.73 ± 0.24	1.08 ± 0.43	1.38 ± 0.12	1.48 ± 0.07	1.62 ± 0.05	0.69 ± 0.22	0.23 ± 0.06	0.21 ± 0.03
D _{Tl}	0.3 ± 0.1	0.3 ± 0.1	0.2 ± 0.1	5.1 ± 0.6	10.7 ± 1.4	0.9 ± 1.8	0.9 ± 0.5	3.7 ± 0.8	5.9 ± 0.9
logK ^{D_{Tl}}	-1.17 ± 0.14	-1.08 ± 0.20	-1.28 ± 0.16	0.17 ± 0.05	0.35 ± 0.06	0.45 ± 0.06	-0.55 ± 0.21	0.13 ± 0.10	0.38 ± 0.07
ΔIW	-2.39	-2.19	-2.01	-2.17	-2.71	-2.66	-2.07	-1.87	-1.65

Table 2 (continued)

Experiment	Z1820	Z1821	Z1823	Z1824	Z1825	Z1956	Z1957	Z1959
Starting material	B	A	A	A	B	A	B	A
Pressure (GPa)	7	7	14	18	18	20	20	16
Temperature (K)	1979	2023	2573	2473	2473	2573	2573	2473
Duration (min)	10	1	1	4	4	1	1	1
Pressure media	MgO+Cr ₂ O ₃							
Capsule	MgO SC							
Silicate composition (oxide wt.%)								
n	13	19	13	9	22	15	13	15
SiO ₂	35.29 ± 0.90	48.54 ± 1.04	39.39 ± 0.55	44.82 ± 0.35	39.16 ± 0.16	39.45 ± 0.68	39.90 ± 0.34	37.78 ± 0.43
Al ₂ O ₃	9.72 ± 1.25	12.07 ± 0.58	9.09 ± 0.29	14.12 ± 0.95	8.83 ± 0.14	9.32 ± 0.07	8.93 ± 0.07	9.73 ± 0.11
CaO	6.96 ± 0.99	12.33 ± 0.41	9.10 ± 0.45	10.32 ± 0.07	9.69 ± 0.10	9.36 ± 0.26	9.48 ± 0.21	8.98 ± 0.24
MgO	35.89 ± 1.86	15.35 ± 0.30	35.61 ± 0.91	23.44 ± 0.37	30.42 ± 0.18	33.36 ± 0.97	31.53 ± 0.51	36.88 ± 0.68
FeO	9.98 ± 0.26	8.45 ± 0.54	5.99 ± 0.12	4.86 ± 0.45	7.79 ± 0.07	6.15 ± 0.14	6.52 ± 0.11	5.93 ± 0.12
Na ₂ O	0.69 ± 0.11	1.75 ± 0.14	1.16 ± 0.04	1.00 ± 0.16	1.06 ± 0.03	1.34 ± 0.03	1.26 ± 0.03	1.11 ± 0.03
TiO ₂	0.70 ± 0.10	0.78 ± 0.08	0.68 ± 0.04	0.77 ± 0.07	0.82 ± 0.03	0.72 ± 0.02	0.67 ± 0.04	0.73 ± 0.02
K ₂ O	0.22 ± 0.03	0.10 ± 0.02	0.14 ± 0.01	0.11 ± 0.02	0.14 ± 0.01	0.15 ± 0.01	0.12 ± 0.005	0.12 ± 0.01
P ₂ O ₅	0.08 ± 0.01	0.02 ± 0.005	0.01 ± 0.000	0.01 ± 0.001	0.09 ± 0.02	0.01 ± 0.000	0.04 ± 0.002	0.01 ± 0.000
SO ₂	0.16 ± 0.02	0.01 ± 0.001	0.01 ± 0.001	0.002 ± 0.001	0.11 ± 0.01	0.01 ± 0.001	0.27 ± 0.01	0.01 ± 0.001
Total	100.10 ± 0.60	100.03 ± 0.98	101.73 ± 0.21	100.22 ± 0.21	99.99 ± 0.26	100.56 ± 0.18	99.99 ± 0.16	101.88 ± 0.11
Sn (ppm)	1385 ± 65	368 ± 151	272 ± 8	208 ± 20	2497 ± 258	259 ± 72	2407 ± 415	250 ± 34
Cd (ppm)	2119 ± 432	3761 ± 1037	1966 ± 48	3673 ± 211	3490 ± 250	2991 ± 749	2564 ± 517	2626 ± 50
Bi (ppm)	35 ± 6	126 ± 105	52 ± 4	50 ± 12	157 ± 46	54 ± 15	183 ± 30	64 ± 16
Sb (ppm)	72 ± 18	19 ± 8	10 ± 2	5 ± 1	144 ± 80	10 ± 3	113 ± 19	22 ± 13
Tl (ppm)	2348 ± 119	5875 ± 3597	1098 ± 291	609 ± 66	733 ± 449	622 ± 184	1133 ± 205	841 ± 50
Metal composition (wt.%)								
n	10	18	39	33	43	19	16	9
Fe	59.99 ± 1.32	87.00 ± 0.60	78.02 ± 0.50	78.77 ± 0.35	63.29 ± 0.35	78.26 ± 0.82	62.90 ± 0.82	76.38 ± 5.09
Sn	4.65 ± 0.26	4.80 ± 0.11	5.58 ± 0.09	4.92 ± 0.05	6.35 ± 0.19	4.19 ± 0.31	6.60 ± 0.23	4.24 ± 0.36
P	0.001 ± 0.000	0.17 ± 0.04	0.08 ± 0.005	0.06 ± 0.005	0.01 ± 0.001	0.09 ± 0.01	0.03 ± 0.01	0.06 ± 0.01
S	17.90 ± 0.44	0.32 ± 0.05	0.31 ± 0.01	0.23 ± 0.01	15.91 ± 0.22	0.30 ± 0.02	16.73 ± 0.69	0.23 ± 0.02
Si	0.03 ± 0.001	N.D.	0.05 ± 0.01	0.04 ± 0.005	0.04 ± 0.01	0.23 ± 0.06	0.01 ± 0.01	0.04 ± 0.01
O	1.97 ± 0.18	0.19 ± 0.06	1.25 ± 0.14	0.99 ± 0.13	1.55 ± 0.11	0.36 ± 0.07	1.17 ± 0.35	0.38 ± 0.10
Ti	N.D.	N.D.	N.D.	N.D.	N.D.	0.003 ± 0.001	0.00 ± 0.00	0.000 ± 0.000
Mg	0.09 ± 0.003	0.23 ± 0.06	0.18 ± 0.03	0.13 ± 0.01	0.11 ± 0.02	0.12 ± 0.004	0.41 ± 0.33	0.12 ± 0.01
Cd	1.82 ± 0.28	0.35 ± 0.09	0.73 ± 0.06	0.87 ± 0.05	0.58 ± 0.03	1.42 ± 0.15	0.50 ± 0.07	2.01 ± 1.32
Bi	1.73 ± 0.15	0.37 ± 0.12	1.66 ± 0.09	2.24 ± 0.08	2.44 ± 0.19	2.26 ± 0.17	2.02 ± 0.45	3.47 ± 2.07
Sb	3.01 ± 0.21	2.63 ± 0.12	3.28 ± 0.06	3.25 ± 0.03	3.05 ± 0.08	4.30 ± 0.34	3.47 ± 0.23	3.29 ± 0.21
Tl	1.04 ± 0.11	0.32 ± 0.07	1.82 ± 0.16	1.73 ± 0.09	0.01 ± 0.005	2.03 ± 0.14	0.17 ± 0.07	2.26 ± 1.53
Total	98.17 ± 0.13	99.99 ± 0.68	98.15 ± 0.28	98.03 ± 0.13	98.07 ± 0.18	98.48 ± 0.32	96.85 ± 0.33	98.55 ± 0.43
D _{Ca}	8.8 ± 2.2	1.0 ± 0.4	4.5 ± 0.4	2.7 ± 0.2	1.7 ± 0.1	5.8 ± 1.6	2.0 ± 0.5	9.7 ± 6.3
logK ^D _{Ca}	0.05 ± 0.11	-1.14 ± 0.16	-0.65 ± 0.04	-0.96 ± 0.05	-0.80 ± 0.04	-0.54 ± 0.12	-0.81 ± 0.11	-0.34 ± 0.29
D _{Bi}	513 ± 96	32 ± 28	380 ± 38	507 ± 127	157 ± 48	510 ± 150	113 ± 32	690 ± 447
logK ^D _{Bi}	1.36 ± 0.08	-0.23 ± 0.39	0.62 ± 0.04	0.63 ± 0.12	0.65 ± 0.13	0.75 ± 0.13	0.39 ± 0.12	0.85 ± 0.28
D _{Sb}	428 ± 109	1497 ± 646	3870 ± 771	6935 ± 1198	213 ± 118	5146 ± 1676	312 ± 56	1904 ± 1142
logK ^D _{Sb}	1.28 ± 0.11	1.45 ± 0.19	1.63 ± 0.09	1.77 ± 0.09	0.79 ± 0.24	1.76 ± 0.14	0.83 ± 0.08	1.29 ± 0.26
D _h	4.5 ± 0.5	0.6 ± 0.4	20.0 ± 5.6	32.1 ± 3.9	0.2 ± 0.1	39.6 ± 12.1	1.5 ± 0.7	33.9 ± 23.1
logK ^D _h	0.21 ± 0.05	-0.81 ± 0.29	0.65 ± 0.12	0.82 ± 0.07	-1.28 ± 0.33	0.95 ± 0.13	-0.36 ± 0.20	0.87 ± 0.30
ΔIW	-1.80	-2.30	-2.61	-2.76	-2.06	-2.61	-2.22	-2.65

Table 3: Summary of regression parameters calculated for Cd, Bi, Sb and Tl using experiments of this study and literature data.

Parameter	Cd	Bi	Sb	Tl
a	-0.63 ± 0.21	-7.05 ± 1.04	-5.41 ± 0.99	2.88 ± 0.65
b	–	$14\,037 \pm 2\,020$	$14\,870 \pm 1\,745$	$-7\,010 \pm 1\,200$
c	–	308 ± 40	193 ± 61	101 ± 28
ε_M^S	-4.29 ± 0.27 (below 18 GPa)	-4.11 ± 1.07 (below 3 GPa)	10.48 ± 0.66	-7.21 ± 0.32 (below 7 GPa) 9.79 ± 1.50 (above 10 GPa)

Table 4: Compilation of apparent partition coefficients inferred from CI and BSE measurements.

MSVE	Cd	Bi	Sb	Tl
T50 (K) ^a	652	746	979	532
T50 (K) ^b	502	480	890	365
BSE	64 ^d	5 ^d	12 ^d	3.5 ^e
±	19	2.5	4	1.4
CI	675 ^a	110 ^a	152 ^a	143 ^a
±	6	3	9	2
Core/BSE ^a	7.1	17.2	11.8	19.2
±	4.4	11.7	4.1	18.6
Lithophile reference element	F ^{a,d}	F ^{a,d}	Na ^{a,d}	I ^f
Core/BSE ^b	2.6	7.6	11.1	19.2
±	2.6	6.4	3.9	18.6
Lithophile reference element	Cl ^f	Cl ^f	K ^{a,d}	I ^f
Core/BSE ^c	8.6	15	–	14
Range	0–11.5	1.2–28.9	7.2–15.9	0.6–37.8

^aLodders (2003); ^bWood et al. (2019); ^cBraukmüller et al. (2019); ^dPalme and O'Neill (2003); ^eMcDonough and Sun (1995); ^fClay et al. (2017)